

AFRL-RY-HS-TR-2009-0020



DISTRIBUTED ARRAYS AND SIGNAL PROCESSING FOR THE TECHSAT21 SPACE-BASED RADAR

Hans Steyskal, John K. Schindler
Sensors Directorate (RYHA)
Air Force Research Laboratory
80 Scott Drive
Hanscom AFB, MA 01731

In-House Technical Report
April 2009

APPROVED FOR PUBLIC RELEASE - DISTRIBUTION UNLIMITED


AIR FORCE RESEARCH LABORATORY
Sensors Directorate
Electromagnetics Technology Division
80 Scott Drive
Hanscom AFB MA 01731-2909

NOTICE AND SIGNATURE PAGE

Using Government drawings, specifications, or other data included in this document for any purpose other than Government procurement does not in any way obligate the U.S. Government. The fact that the Government formulated or supplied the drawings, specifications, or other data does not license the holder or any other person or corporation; or convey any rights or permission to manufacture, use, or sell any patented invention that may relate to them.

This report was cleared for public release by the Electronic Systems Center Public Affairs Office for the Air Force Research Laboratory Electromagnetic Technology Division and is available to the general public, including foreign nationals. Copies may be obtained from the Defense Technical Information Center (DTIC) (<http://www.dtic.mil>).

AFRL-RY-HS-TR-2009-0020 HAS BEEN REVIEWED AND IS APPROVED FOR PUBLICATION IN ACCORDANCE WITH ASSIGNED DISTRIBUTION STATEMENT.



DAVID D. CURTIS
Branch Chief
Antenna Technology



ROBERT V. MCGAHAN
Technical Communications Advisor
Electromagnetics Technology Division

This report is published in the interest of scientific and technical information exchange, and its publication does not constitute the Government's approval or disapproval of its ideas or findings.

REPORT DOCUMENTATION PAGEForm Approved
OMB No. 0704-0188

Public reporting burden for this collection of information is estimated to average 1 hour per response, including the time for reviewing instructions, searching existing data sources, gathering and maintaining the data needed, and completing and reviewing this collection of information. Send comments regarding this burden estimate or any other aspect of this collection of information, including suggestions for reducing this burden to Department of Defense, Washington Headquarters Services, Directorate for Information Operations and Reports (0704-0188), 1215 Jefferson Davis Highway, Suite 1204, Arlington, VA 22202-4302. Respondents should be aware that notwithstanding any other provision of law, no person shall be subject to any penalty for failing to comply with a collection of information if it does not display a currently valid OMB control number. PLEASE DO NOT RETURN YOUR FORM TO THE ABOVE ADDRESS.

1. REPORT DATE (DD-MM-YYYY) 30 April 2009		2. REPORT TYPE Final Report		3. DATES COVERED (From - To) 1 May 2003 – 1 May 2009	
4. TITLE AND SUBTITLE Distributed Arrays and Signal Processing for the TechSat21 Space-Based Radar				5a. CONTRACT NUMBER	
				5b. GRANT NUMBER	
				5c. PROGRAM ELEMENT NUMBER 61101F	
6. AUTHOR(S) Hans Steyskal, John K. Schindler				5d. PROJECT NUMBER 2304	
				5e. TASK NUMBER HA	
				5f. WORK UNIT NUMBER 01	
7. PERFORMING ORGANIZATION NAME(S) AND ADDRESS(ES) Electromagnetics Technology Division /Sensors Directorate Air Force Research Laboratory 80 Scott Drive, Hanscom AFB MA 01731-2909				8. PERFORMING ORGANIZATION REPORT	
9. SPONSORING / MONITORING AGENCY NAME(S) AND ADDRESS(ES) Air Force Office of Scientific Research 875 N. Randolph St., Suite 325 Arlington, VA 22203				10. SPONSOR/MONITOR'S ACRONYM(S) AFRL/RHYA	
				11. SPONSOR/MONITOR'S REPORT NUMBER(S) AFRL-RY-HS-TR-2009-0020	
12. DISTRIBUTION / AVAILABILITY STATEMENT APPROVED FOR PUBLIC RELEASE, DISTRIBUTION UNLIMITED. 66 ABW-2009-1214 23 OCT 2009					
13. SUPPLEMENTARY NOTES					
14. ABSTRACT The TechSat21 space-based radar concept, suggested by AFRL/VS, employs a cluster of free-floating satellites, each of which transmits its own orthogonal signal and receives all reflected signals. The satellites operate coherently at X-band. The cluster forms essentially a multi-element interferometer with a concomitant large number of grating lobes and significant ground clutter. This study explores some basic characteristics of such a system with respect to detection of slowly-moving ground targets (GMTI).					
15. SUBJECT TERMS Space-borne radar, pulse Doppler radar, antenna array, space-time pattern synthesis, multi-element interferometer, MTI					
16. SECURITY CLASSIFICATION OF:			17. LIMITATION OF ABSTRACT U	18. NUMBER OF PAGES 50	19a. NAME OF RESPONSIBLE PERSON David Curtis, Chief AFRL/RHYA
a. REPORT Unclassified	b. ABSTRACT Unclassified	c. THIS PAGE Unclassified			19b. TELEPHONE NUMBER (include area code) 781-377-2049

Standard Form 298 (Rev. 8-98)
Prescribed by ANSI Std. Z39.18

Table of Contents

<u>Section</u>	<u>Page</u>
List of Figures	iii
List of Tables	iv
Preface.....	v
Acknowledgements.....	vii
Summary	viii
1. Introduction of the TechSat21 Space-Based Radar System	1
2. Basic Considerations.....	1
3. Application to TechSat21	4
4. Comparison with Randomly Thinned Array.....	10
5. Performance of the Rotating Array.....	11
7. Comparison with General Space-Time Processing.....	12
8. Performance of the Planar Array under Non-Ideal Conditions	13
8.1 The Effects of Array Pitch and Yaw.....	21
8.2 Effects of Random Position Errors.....	22
9. Conclusions.....	16
10. References.....	19
Appendix A: Comparison of Target Detection for Two Different Radar Modes.....	21
Appendix B: The Doppler Spectrum for Moving Targets and Clutter	23
Appendix C: Optimization of the Array Element Weights.....	28
Appendix D: Doppler Filter Optimization.....	32
Appendix E: Optimization of Space-Time Filter.....	35
Appendix F: Satellite Position Accuracy.....	38

List of Figures

<u>Figure</u>	<u>Page</u>
1. The TechSat21 space-based radar employs a cluster of small free-floating satellites. Each satellite transmits its own unique signal and receives all reflected signals from the target.	1
2. Target return and ground clutter return in Angle-Doppler space.	3
3. Clutter Doppler spectrum received with fully filled array (blue/green), with thinned periodic (blue) and thinned random arrays (red solid ensemble average, red dashed one realization)...	3
4. Incident clutter Doppler spectrum, Doppler filter transfer function and resultant output power spectrum.	4
5a. Separable signal processing - array beamformer followed by Doppler filter provides M+N degrees of freedom for Signal/Clutter optimization.....	5
5b. Full space-time processing provides MxN degrees of freedom.....	5
6a. Vertical array in Earth orbit, viewed end-on. Array scans 30°- 60° off broadside.....	5
6b. Array Geometry: 19-Element Array in Triangular Grid.	5
7. Illustration of the orbital geometry chosen for the numerical examples	6
8a. Configuration of 19-element sparse array and contour plot of the array pattern (contours at -3dB, -10dB, -20dB). Horizontal centerline represents desired range bin mapped onto the pattern, upper and lower lines represent aliased range bins. Array rotation angle = 0°	7
8b. As in 8a, but array rotated through an angle = 15°,	7
9. Doppler spectrum of received ground clutter, corresponding to two-way array pattern. The envelope represents the element pattern.	8
10. Aliased Doppler spectrum. Pulse repetition frequency f_{rep} chosen such that the fourth grating lobe in Fig. 8 aliases onto main beam ($f_{rep} = 4640$ Hz).	8
11. Clutter suppression with an N-pulse canceller; “filter” is the power transfer function of the canceller; “clutter ‘in’” and “clutter ‘out’” represent clutter power spectrum at the input and output of the canceller: two-pulse canceller ($N = 2$, $N_t = 4$) at top; three-pulse canceller ($N = 3$, $N_t = 4$) at bottom.	10
12. Signal/Clutter improvement factor vs. array rotation angle (top), and corresponding pulse repetition frequency (bottom).	11
13. Signal/Clutter improvement factor vs. filter order for various alternatives of optimization.	12
14. Comparison of Signal/Clutter improvement factors achievable with a periodic array and array with periodicity spoiled by random but known errors (two realizations).....	13

15. Improvement factor vs. pulse repetition frequency for the 19-element array with 0 deg. pitch, 0 deg yaw (top), and 5 deg. pitch, 0 deg. yaw (bottom).	14
16. Improvement factor vs. pulse repetition frequency for the 19-element array with 0 deg. pitch, and yaw corresponding to Earth rotation.	15
17. The improvement factor vs. pulse repetition frequency for random position errors within boxes 1, 3, and 5 m on the side (0 deg. pitch, 0 deg. yaw).	17
18. Improvement factor vs. pulse repetition frequency for the case of array pitch =5° , yaw according to Earth rotation, and increasing element position errors.	18
A 1. The element beamwidth Ω_o is much wider than the array beamwidth Ω_a . Surveillance of a radar sector $\Omega_s = \Omega_o$ requires Ω_o/Ω_a beams.	22
B 1. Illustration of radar and moving target geometry.	23
B 2. Target return and ground clutter return in Angle-Doppler space.	24
B 3. Illustrating the derivation of minimum aperture size and coherent integration time.	25
B 4. Global coordinate system and satellite-based coordinate system used in the computation of the clutter Doppler frequency (r_s and v_s are unit vectors along the radial direction to the satellite and along the satellite velocity, respectively, and $n_s=r_s \times v_s$).	27
C 1. Array beamformer with weights a_m followed by Doppler filter with weights w_n	28
D 1. Array with Doppler filter.	32
E 1. Array with full space-time filter.	35
F 1. Maximum control error, ϵ , in meters vs. the satellite along track aperture, in meters, to insure that average sparse array grating lobes within the aperture main beam decrease less than 3 dB.	39

List of Tables

<u>Table</u>	<u>Page</u>
1. Processing gain SCR_{out}/SCR_{in} (dB).....	17

Preface

On two occasions, the U.S. Air Force research and development community has proposed multi-function space-based sensor concepts that employ a formation of identical, free-floating, semi-autonomous, and self-organizing micro-satellites to form large space apertures [1,2]. In view of recent advances in space-time processing, we consider here the design principles, performance, and technical risks associated with such a network of satellites that function collaboratively as a distributed array radar for detecting and tracking moving objects near the earth surface.

The satellite network is viewed as a cost-effective approach to achieve the large apertures in space required for detecting slowly-moving targets with a rapidly-moving satellite array. Cost effectiveness is envisioned from efficient mass production of nearly identical micro satellites, opportunistic launch and gradual network formation, and maintenance and performance enhancement through gradual replacement of network satellites during mission lifetime with residual space launch capacity. In addition, the satellite network can conceivably accomplish multiple missions via reconfiguration to provide passive, interferometric emitter location, local and wide area communications, and a variety of radar functions including synthetic aperture radar mapping and detection and tracking of targets moving with respect to the earth surface. In this work, we analyze the wide-area radar detection of slowly moving targets, perhaps the most technically demanding of the potential radar missions for the distributed sensor array.

There are myriad technical problems associated with distributed networks of autonomous satellites that must function collaboratively to accomplish a common mission. Formation flying is one problem. The satellites must navigate in the formation with knowledge of the common array mission and information on the locations of other satellites in the formation to avoid collisions and, desirably, to obtain proper formation positions with adequate precision during the mission observation time. Navigation must be achieved with minimum energy consumption to extend the life of network satellites. A second problem is achieving collaborative behavior of the satellites toward the common array mission. The architecture for centralized mission planning with distributed satellite control must be refined. High speed inter-satellite data communications are necessary to (1) effectively locate each satellite in space from inter-satellite range measurements, (2) achieve common transmit and receive signal timing and coherence for sparse array beamforming and signal processing, and (3) implement transmit waveform selection and scheduling and array processing for beamforming and receive signal processing. Finally, a third problem is associated with the performance of a search radar operating against ground reflections or clutter when implemented with a large, coherent, highly-thinned array on transmit and receive. The large, sparse, multi-element time-varying phased array can form a narrow beamwidth array pattern with concomitant grating and random sidelobes that introduce significant ground clutter into the receive signal.

Previous work described approaches to distributed space-based radar employing satellites in a single orbit [3-7]. This report summarizes our work [8-11] on a more advanced system, which employs a cluster of free-floating satellites in a unique periodic constellation. The geometry is such that orbital mechanics maintains cluster periodicity as the cluster orbits the Earth. The satellites have identical phased array antennas for transmit and receive, and each satellite transmits its own, possibly orthogonal, signal and receives the reflected signals from all

transmitting satellites, similar to the French RIAS groundbased system [12-14]. Thus the system constitutes a full multiple-input multiple-output (MIMO) system.

Later we investigated signal processing techniques and GMTI performance of more general linear and planar random arrays [15-17]. These results will be published in a companion report [18]. For a linear array that moves along its axis, it is shown that the optimum space-time processing leads to a solution that is similar to a displaced-phase-center antenna (DPCA).

Acknowledgements

The US Air Force Office of Scientific Research supported this study under Dr. Arje Nachman. We gratefully acknowledge the contributions to this work of Dr. Robert Mailloux, Dr. Peter Franchi, and Dr. Scott Santarelli.

Summary

The TechSat21 space-based radar concept, suggested by AFRL/VS, employs a cluster of free-floating satellites, each of which transmits its own orthogonal signal and receives all reflected signals. The satellites operate coherently at X-band. The cluster forms essentially a multi-element interferometer with a concomitant large number of grating lobes and significant ground clutter. This study explores some basic characteristics of such a system with respect to detection of slowly-moving ground targets (GMTI).

A companion report [18] investigates the GMTI performance of basic random sparse arrays. For a linear array which moves along its axis, it is shown that the optimum space-time processing leads to a solution that is similar to a displaced-phase-center antenna (DPCA).

In this report we propose a novel two-dimensional periodic array geometry for TechSat21 and an associated technique for pattern synthesis in angle-frequency space. It exploits the double periodicities of the grating lobes in the angular domain and of the radar pulses in the frequency domain, and allows substantial gains in clutter suppression.

We consider a 'separable' system architecture for TechSat21, where a planar M -element array is followed by a single N -pulse Doppler filter, and evaluate some processing alternatives for their effectiveness in clutter suppression. An attractive feature of this architecture is that it allows simple, multi-pulse MTI processing and adaptive antenna pattern control. The limited number of degrees of freedom, $M+N$, requires a relatively low computational load. General space-time processing is also evaluated and shown to offer substantially improved signal/clutter ratios. However, the larger number of degrees of freedom, $M \times N$, implies a heavy computational load.

Finally, taking the ideal periodic array as a reference case, we analyze the performance degradation with array pitch (satellite cluster rotation) and yaw (Earth rotation), and known random element position errors. It is found that the signal/interference improvement factor is an extremely sensitive function of the pulse repetition frequency and that it varies over a large dynamic range. Achievable improvement factor maxima are moderately degraded by array pitch and strongly degraded with increasing position errors. Yaw effects appear to be negligible. In general, with increased randomness, fewer elements contribute to form DPCA pairs so that satellite usage efficiency (and SNR) is degraded.

Thus, a periodic array lattice allows for significantly better clutter suppression than a non-periodic lattice, independent of the particular space-time processing scheme.

1. Introduction of the TechSat21 Space-Based Radar System

The space-based radar concept TechSat21 [2,19,20] is based on a distributed cluster of free-floating, small satellites operating cooperatively to perform a surveillance mission. The primary focus is the Moving Target Indication (MTI) radar mode. A baseline assumption is, similar to the French RIAS system [12-14], that the individual satellites transmit different frequencies (or other orthogonal signals), but receive all the reflected signals at the frequencies transmitted by the other satellites in the cluster, as shown in Fig. 1. In addition, it is assumed that the positional accuracy can be sensed to within a fraction of a wavelength so that signals can be combined coherently. The apparent loss of array gain on transmit does not degrade radar target detection, as explained in Appendix A. Each satellite has roughly a 4 m^2 phased array operating at about 10 GHz, other typical parameters are 4 to 20 satellites per cluster, cluster diameters 100 to 1000 meters, and orbits 700 to 1000 km above Earth.

Our companion report [18] considers moving target detection with a linear, random array to derive the fundamental characteristics and provide insight. In the present report we summarize our earlier work on the performance of a more specific space-based radar system with a sparse two-dimensional array in a circular low Earth orbit. Other approaches to distributed space-based radar employing satellites in a single orbital plane are described in [3,4,6,7]. We discuss a particular array geometry, analyze its pattern foot print on a spherical Earth, present results of clutter suppression for signal processing techniques of various levels of complexity, analyze the sensitivity to pulse repetition frequency (prf), and, finally, determine the effects of various array errors.

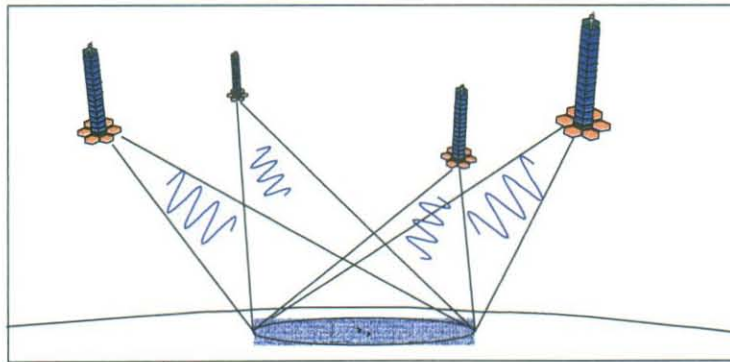


Figure 1. The TechSat21 space-based radar employs a cluster of small free-floating satellites. Each satellite transmits its own unique signal and receives all reflected signals from the target.

2. Basic Considerations

Detection of a slowly-moving ground target by a moving radar is based on the difference of the Doppler frequencies of the target return and the ground clutter. The situation is depicted in Fig. 2, where the ground clutter ridge f_{clutter} is the return from one range bin illuminated by the antenna main beam and sidelobes. The different angular parts of the range bin generate an extended Doppler spectrum, since they have radial velocities that vary with azimuth angle ϕ as seen from the radar. A moving target in the antenna main beam appears as a spike in the angle-Doppler

domain. To separate the target return from the clutter ridge clearly requires a narrow antenna main beam and a narrow Doppler filter bandwidth, or equivalently, a minimum aperture dimension A and coherent integration time T . These are shown in Appendix B to be

$$A \approx \frac{3}{2} \frac{v_{\text{radar}}}{v_{\text{target}}} \lambda, \quad T \approx \frac{3}{4} \frac{\lambda}{v_{\text{target}}}, \quad (1)$$

where v_{target} is the target speed, v_{radar} the radar along track speed, and λ the radar wavelength. (Effects of the illumination angle and the velocity directions can increase these minimum requirements but have been suppressed, as discussed in Appendix B). Sampling the aperture A at $\lambda/2$ spacing leads to a total number of spatial samples (array elements)

$$N_S = 3 \frac{v_{\text{radar}}}{v_{\text{target}}}. \quad (2a)$$

Similarly, over the time T , the total number of temporal samples

$$N_T = 3 \frac{v_{\text{radar}}}{v_{\text{target}}}, \quad (2b)$$

since the minimum temporal sampling rate equals twice the highest Doppler frequency $2 v_{\text{radar}}/\lambda$.

It is interesting to note that the total numbers of spatial and temporal samples are equal, and that they are determined solely by the ratio of $v_{\text{radar}}/v_{\text{target}}$, independent of the radar frequency. However, for slowly-moving targets viewed from space these numbers are large. For example, a target speed $v_{\text{target}} = 2.2$ m/s (8 km/hour) and a low Earth orbit radar speed $v_{\text{radar}} = 7500$ m/s leads to

$$N_A = N_T = 10^4, \quad (3)$$

corresponding to a (linear) array with 10000 elements that generates 10^8 space-time samples at each range sample for unambiguous azimuth-Doppler processing. With 100 range bins and a prf = 1000 this represents a data rate of 10^{13} samples per second. It is obvious that the narrow beamwidth and long processing times can slow the search rate of such a radar system and the large number of space-time samples present a substantial signal processing requirement. Thus there is a strong motivation for reducing the number of samples, i.e. for spatial and temporal undersampling.

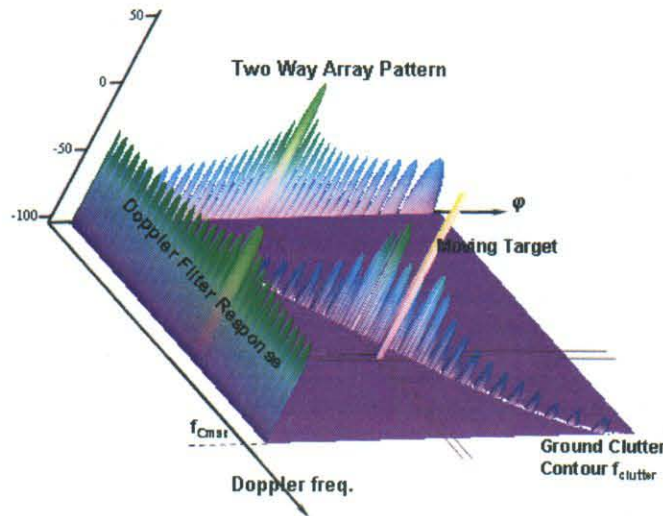


Figure 2. Target return and ground clutter return in Angle-Doppler space.

A spatially undersampled or thinned array maintains the narrow beamwidth necessary for slow moving target detection but introduces excess clutter associated with the lost sidelobe control. Basically, thinning can be periodic or random, which leads to very different sidelobe structures and received clutter Doppler spectra, as seen in Fig. 3. Here equal transmit and receive patterns are assumed. As reference, the clutter spectrum corresponding to a fully filled array is shown. It decreases monotonically away from the main beam, corresponding to the continuous decrease of the sidelobe envelope. Further shown is the spectrum corresponding to a periodically thinned array, whose grating lobes generate a periodic spectrum. Here the clutter is concentrated to relatively high, narrow spectral bands with low clutter regions between. Finally, there is shown the ensemble average clutter spectrum for a randomly thinned array. The clutter power is concentrated at a Doppler frequency corresponding to the main beam pointing direction with a bandwidth that is comparable to that produced by the fully filled array. Outside the main beam, the power is uniform at a level proportional to $1/N^2$, where N is the number of elements in the array. A single realization of the randomly thinned array is also shown by the dotted curve.

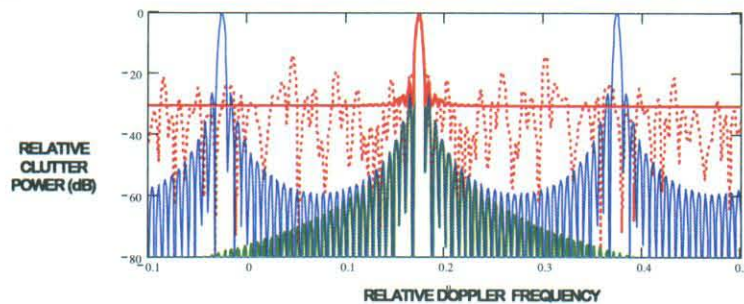


Figure 3. Clutter Doppler spectrum received with fully filled array (blue/green), with thinned periodic (blue) and thinned random arrays (red solid ensemble average, red dashed one realization). Two way propagation is assumed.

The periodically thinned array is preferred since between the harmonic spectral lines, the power spectrum of the clutter is lower than for the random array, permitting better target detectability. In addition, it is compatible with temporal periodic undersampling of this power spectrum. Selecting a sampling frequency (pulse repetition frequency) related to the harmonic spectral lines results in aliases which overlay the original spectral lines, and thus the total spectrum retains the relatively

low clutter power between the spectral lines. Fig. 4 illustrates this point. It shows the power spectrum of a linear, periodically-thinned array along with the power transfer function of a three-pulse binomial canceller, and the resultant uniform residual clutter at the output of the cancellation filter.

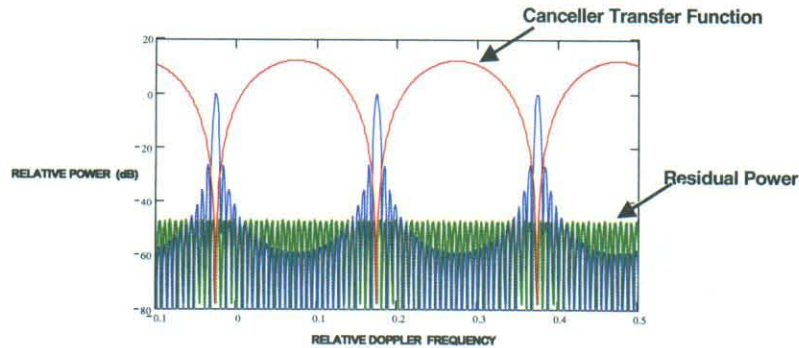


Figure 4. Incident clutter Doppler spectrum, Doppler filter transfer function and resultant output power spectrum.

The array signal processing considered here involves an array beam former followed by a Doppler filter and is denoted as ‘separable’ processing, since it performs spatial and temporal processing independently. Fig. 5a illustrates this separable processing. It is considerably simpler than general space-time processing, where each space-time sample is individually weighted and summed, (see Fig. 5b).

This basic approach of a thinned periodic array with a ‘tuned’ pulse repetition frequency (prf, alt. f_{rep}) and separable processing was initially evaluated for the TechSat21 radar system [8-11]. In a second phase we evaluated also the performance with full space-time processing [15-16].

3. Application to TechSat21

Cluster configurations are governed by orbital mechanics, i.e. Kepler's equations. Linearization for small motions around a reference point in a global circular orbit leads to the Hill equations, derived in 1878, and alternatively named Clohessy-Wiltshire equations, who rederived them in 1960 [20]. These equations constrain the satellites to move either along a linear track or to local orbits around the reference point, such that their projections on a vertical plane form 2:1 ellipses.

Our proposed TechSat21 configuration consists of a vertical, planar, 19-element array as shown in Fig. 6. The vertical orientation allows looking toward both sides equally well and gives the highest gain at maximum range. The array configuration, with one central element and six elements on each of three concentric 2:1 ellipses, realizes a periodic triangular grid. During each Earth orbit the elements rotate one full cycle along their respective ellipses but maintain a

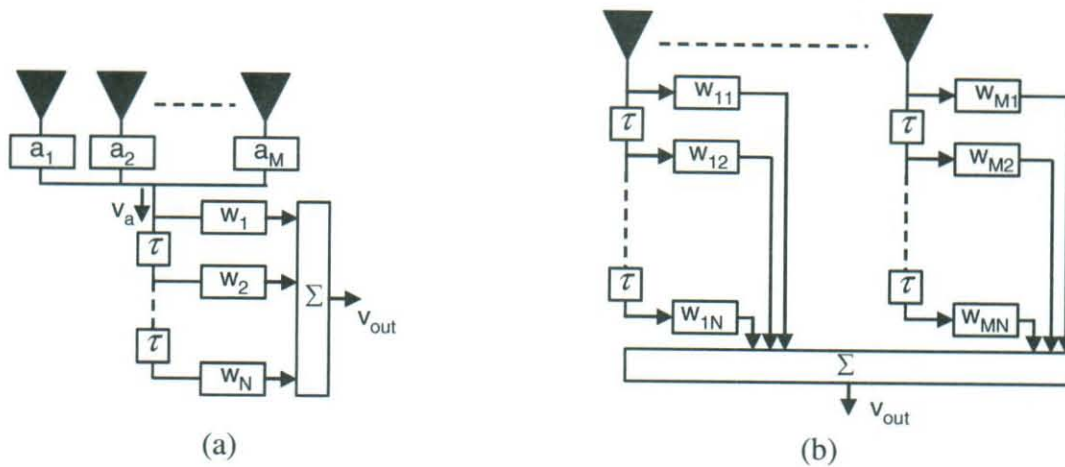


Figure 5. (a) Separable signal processing - array beamformer followed by Doppler filter provides $M+N$ degrees of freedom for Signal/Clutter optimization. (b) Full space-time processing provides $M \times N$ degrees of freedom.

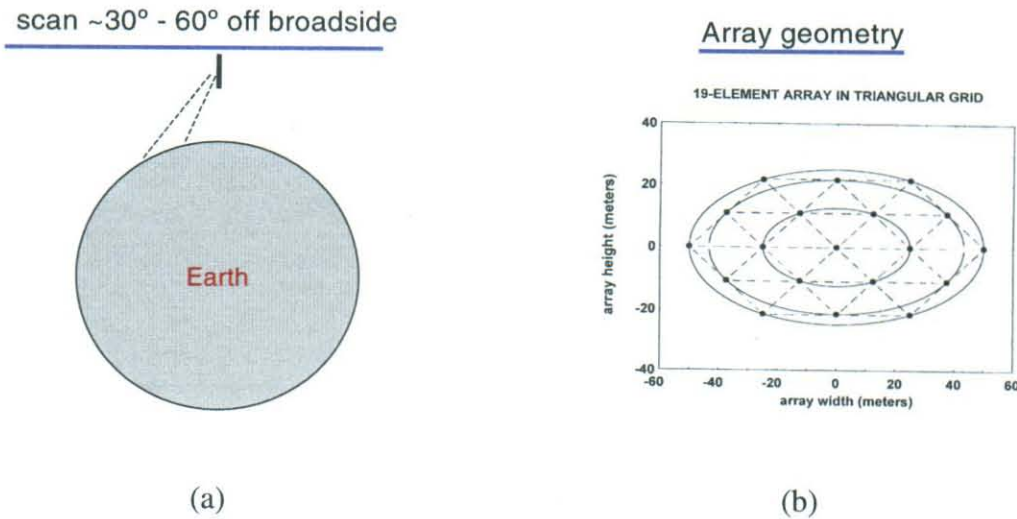


Figure 6. (a) Vertical array in Earth orbit, viewed end-on. Array scans $30^\circ - 60^\circ$ off broadside, (b) Array Geometry: 19-Element Array in Triangular Grid.

triangular grid (the ellipse major axes remains tangential to the circular orbit). The triangular lattice is the key to our approach since it generates grating lobes that are highly periodic in angle, and, from further analysis, periodic in Doppler spectrum as well.

Although simple in principle, the approach is complicated by the curvature and rotation of the Earth. The Doppler frequency of the ground clutter is derived in [18] in terms of the satellite orbit coordinates and the array look direction, and the result is repeated in Appendix B for reference. Since the element pattern (the pattern of an individual satellite) illuminates only a relatively small angular sector of the Earth, the grating lobes and Doppler frequencies all experience the same linear shift, as shown by numerical analyses. A second complication is the rotation of the array around its geometric center, which continuously changes the grating lobe structure. However, this can be accommodated by adjusting the pulse repetition frequency accordingly.

To evaluate the above approach quantitatively, we developed a MATLAB code, which computes the received ground clutter for an array in Low Earth Orbit. Representative results are shown in Figs. 8, 9, and 10, which apply for satellite altitude of 850 km above a rotating Earth, orbital plane inclined 70° relative to the equator, and a satellite position 45° above the equator, as illustrated in Fig. 7. The array operates at 10 GHz. The array shape is elliptical with a 100m major axis, and a 50 m minor axis. The 19 elements are $2 \times 2 \text{ m}^2$ phased arrays, the array rotation angle is 0° and the look angle is 45° straight down. The clutter density is assumed uniform in azimuth.

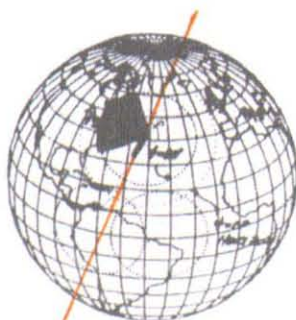


Figure 7. Illustration of the orbital geometry chosen for the numerical examples

Fig. 8 shows the mapping of three range bins onto the array pattern. Due to its particular geometry the range bin maps into a straight line, $u=\text{const.}$, in the array pattern when using the so called sine-space (u,v) -coordinates. The horizontal center line represents the desired range bin and the upper and lower lines represent aliased range bins, corresponding to a pulse time of $2 \mu\text{sec}$ and pulse repetition frequency of 4640 Hz. Note that the aliased bins are illuminated with very low intensity since they fall outside the element pattern (one satellite) and therefore can be ignored. The desired range bin is so narrow in down-range that we consider the pattern constant in this direction, and only consider the cross-range variation when computing the power of the Doppler spectrum received from the ground clutter.

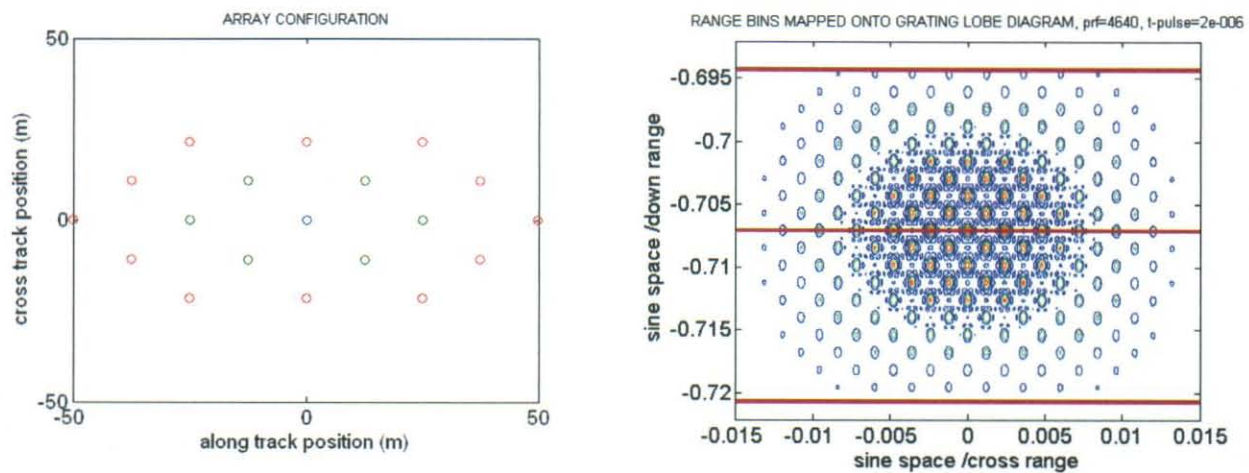


Figure 8a. Configuration of 19-element sparse array and contour plot of the array pattern (contours at -3dB, -10dB, -20dB). Horizontal centerline represents desired range bin mapped onto the pattern, upper and lower lines represent aliased range bins. Array rotation angle = 0°.

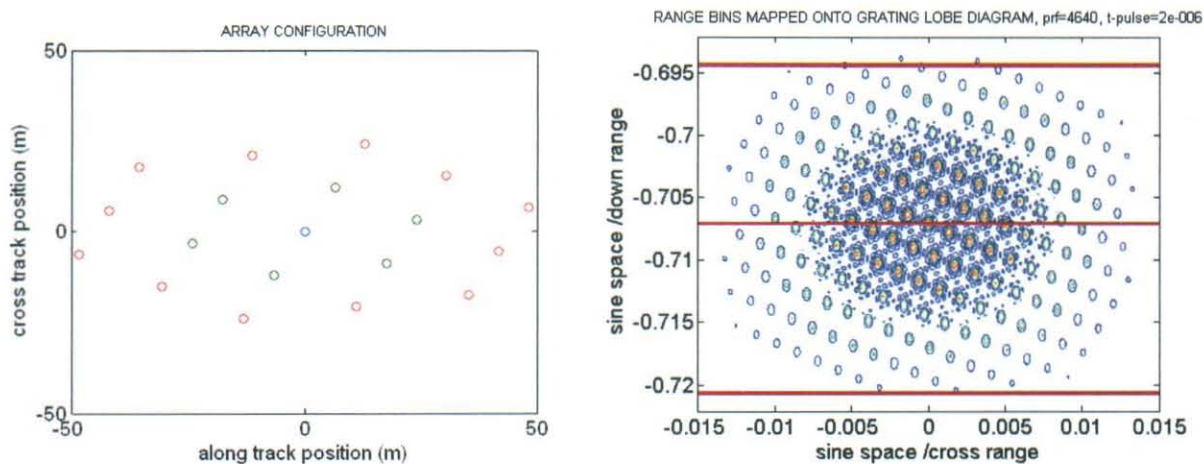


Figure 8b. As above, but array rotated through an angle = 15°.

Fig. 9 shows the main part of the received Doppler spectrum corresponding to the center range bin in Fig. 8. The envelope is determined by the two-way element pattern (one satellite) and is plotted here over an angular sector corresponding to the main beam and ± 3 sidelobes. The narrow 'spikes' are the periodic grating lobes; they are separated by approximately 1160 Hz. A periodic pulse train illumination creates aliasing, and choosing the pulse repetition frequency f_{rep} such that the 4th grating lobe aliases onto the main beam, i.e. $f_{\text{rep}}=4640$ Hz, leads to the Doppler spectrum shown in Fig. 10.

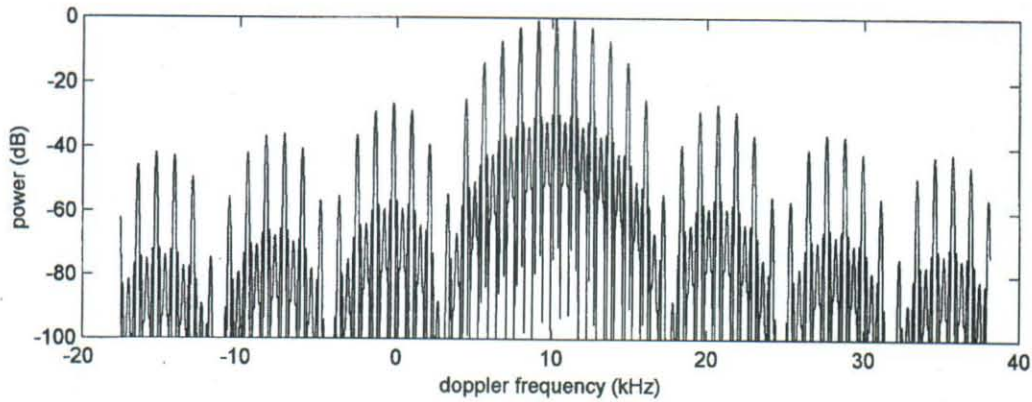


Figure 9. Doppler spectrum of received ground clutter, corresponding to two-way array pattern. The envelope represents the element pattern.

The aliased Doppler spectrum has a period of 4640 Hz. The four apparent 'periods' observed within the 4640 Hz band are due to the periodicity of the grating lobes, and we note that their amplitudes are all practically equal.

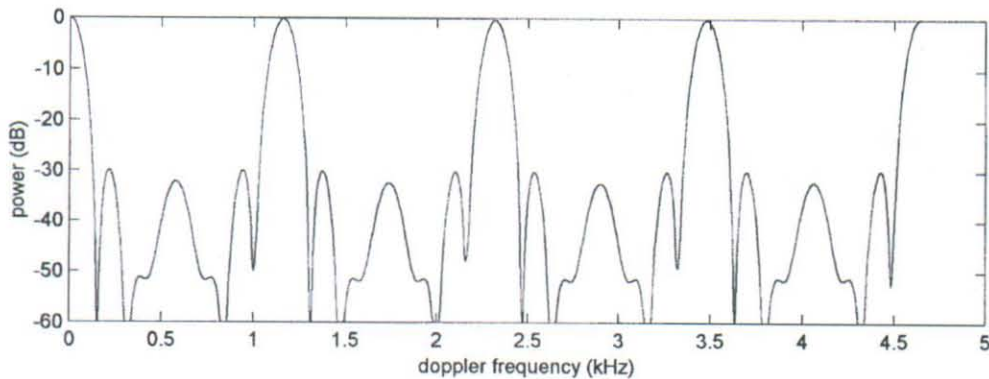


Figure 10. Aliased Doppler spectrum. Pulse repetition frequency f_{rep} chosen such that the 4th grating lobe in Fig. 8 aliases onto main beam ($f_{\text{rep}} = 4640$ Hz).

There is little spreading of the spectral lines associated with each grating lobe, implying significant periodicity of the array grating lobe Doppler frequencies over the beam-width of the satellite array pattern. Also, the spectrum between the grating lobes does not decrease monotonically as with a uniformly illuminated linear array. This is due to the effective amplitude modulation imposed by the two-dimensional vertical aperture.

For moving target indication (MTI) these clutter lines are simply suppressed by an N-pulse canceller and the total power received over the band is then integrated. The canceller, as shown in Fig. 5, provides an output signal

$$s_{out} = \sum_{n=1}^N w_n s_n = s_0 \sum_{n=1}^N w_n e^{j2\pi f_D n \tau}, \quad (4)$$

where w_n denote weights, and the successive radar pulses $s_n = s_0 \exp(j2\pi f_D n \tau)$, with s_0 representing the amplitude of the radar pulse and $2\pi f_D n \tau$ representing the phase shift due to the Doppler frequency f_D of the moving target, and we assume $\tau = 1/f_{rep}$.

Choosing the usual binomial weights for the canceller leads to

$$\sum_{n=1}^N w_n e^{j2\pi f_D n \tau} = \left(1 - e^{j2\pi f_D \tau}\right)^{N-1} \quad (5)$$

or a normalized canceller power transfer function

$$g(f_D) = \sin^{2(N-1)}(\pi f_D \tau) = \sin^{2(N-1)}(\pi f_D / f_{rep}). \quad (6)$$

This function provides nulls at $f_D=0$ and $f_D=f_{rep}$, i.e. one null over the interval $(0, f_D)$. A larger number of evenly spaced nulls, say N_τ nulls, can be obtained with larger time delays $\tau = N_\tau / f_{rep}$, which corresponds to using every N_τ th pulse. The power transfer function becomes

$$g(f_D) = \sin^{2(N-1)}(\pi N_\tau f_D / f_{rep}). \quad (7)$$

Thus we have two parameters to suppress the clutter spectral lines: the number of weights, N , which controls the width of the null and is chosen depending on the aliased grating lobe bandwidth, and the number of pulse intervals, N_τ , which is chosen depending on the number of aliased grating lobes.

We demonstrate the effect of the canceller on the clutter spectrum in the example above, Fig.10. It has four lines and thus we set $N_\tau=4$. Choosing $N=2$ does not quite suppress the clutter lines (see Fig. 11, top), but with $N=3$ we reduce the clutter residue to a fairly uniform level across the whole Doppler band (see Fig.11, bottom). Note that the canceller weights were chosen deterministically using only knowledge of the Doppler frequencies and spectral width of the aliased grating lobes, but without knowledge of other details of the clutter spectrum at the input.

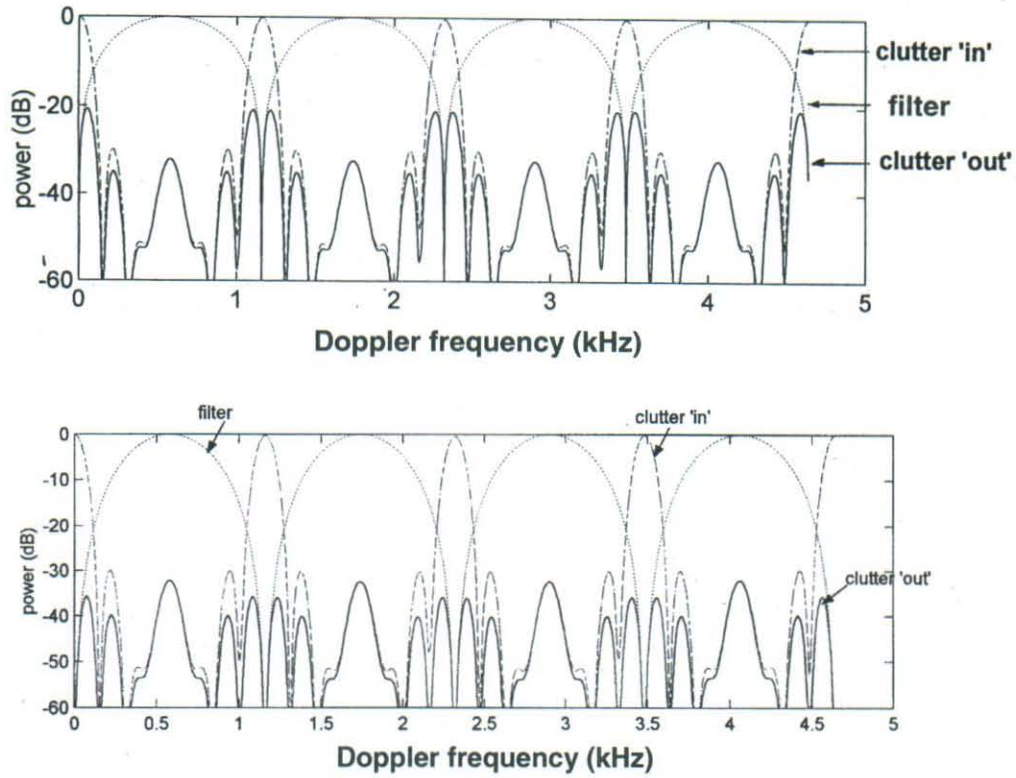


Figure 11. Clutter suppression with an N-pulse canceller; “filter” is the power transfer function of the canceller; “clutter ‘in’” and “clutter ‘out’” represent clutter power spectrum at the input and output of the canceller: 2-pulse canceller ($N = 2$, $N_r = 4$) at top; 3-pulse canceller ($N = 3$, $N_r = 4$) at bottom.

4. Comparison with Randomly Thinned Array

To determine the merit of our approach, we compare it to the standard approach, represented by a 19-element random sparse array. This array has a two-way pattern with smeared sidelobes at an average level $1/(N_{\text{element}})^2 \approx -26$ dB and operates with a non-tailored pulse repetition frequency.

Taking the signal/clutter ratio (SCR) as the performance criterion, we compute the processing gain, i.e. the ratio of SCR_{out} and SCR_{in} at the output and input of the N-pulse cancellers for different numbers N, as shown in Table 1. For the standard approach the processing gain is practically independent of the number of processed pulses, since the sidelobe pattern and thus the clutter Doppler spectrum are essentially flat. Our approach gives a 7 to 17 dB advantage since the clutter is concentrated around a few narrow Doppler lines and can be selectively suppressed.

No. of pulses N	2	3	4
Novel approach	16.3	25.5	26.7
Standard approach	9.6	9.7	9.8
Δ dB	6.7	15.8	16.9

Table 1. Processing gain $SCR_{\text{out}}/SCR_{\text{in}}$ (dB)

5. Performance of the Rotating Array

The above examples were all given for the elliptical array at an array rotation angle $\phi_a = 0^\circ$, i.e. the situation shown in Fig. 6b with five elements on the major axes of the ellipses. This represents the best periodic case. However, during one Earth orbit, the array rotates 360° around its center and changes its triangular grid and thus its grating lobe structure. Therefore, we also evaluated performance for other array rotation angles ϕ_a , over the range $0 \leq \phi_a \leq 30^\circ$ in 2.5° increments, after which the array configuration repeats due to symmetry.

We found that we can always select a basic pulse repetition frequency that leads to signal-to-clutter (S/C) improvement factors around 25 dB. Fig. 12 shows these improvement factors and the corresponding PRFs that maximize signal to clutter. Here S/C improvement was defined as S/C at the filter output relative to S/C at the single receive element, assuming target Doppler frequency to be uniformly distributed between 0 Hz and PRF, and the filter being a binomial, 5-pulse canceller. Multiples of these basic PRFs give the same result and thus our approach is robust with respect to both array rotation angle and PRF.

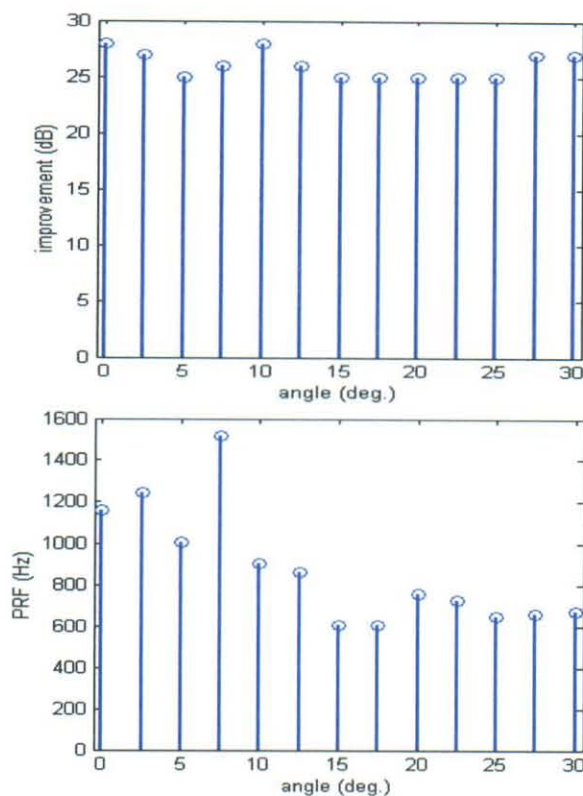


Figure 12. Signal/Clutter improvement factor vs. array rotation angle (top), and corresponding pulse repetition frequency (bottom).

6. Optimization of Separable Space-Time Processing

Our proposed approach for separable space-time processing has M receive element weights a_m and N filter weights w_n , (see Fig. 5a), which in the examples above were chosen corresponding to a maximum gain array, (i.e. $a_m=1$), and to a classical N -pulse canceller, (i.e. w_n =binomial coefficients), respectively. However, these weights can be chosen so as to maximize the S/C improvement factor. Optimizing either the weights a_m or the weights w_n leads to a ratio of quadratic forms in terms of these weights, which has a well-known maximum solution [22].

We have performed such computations for various filter orders and the array rotation angles, $\phi_a=0^\circ$ and $\phi_a=5^\circ$, which represent best and worst cases, respectively. The results are shown in Fig. 13. We note that array optimization is considerably more effective than filter optimization. Also, apparently the N -pulse canceller matches optimum weighting for low filter orders (2-4 pulses) but degrades for higher orders. This is because the deterministic weights place nulls only over the dominant Doppler lines. Once these first order contributors have been suppressed to a uniform level, additional nulls at these locations will not improve the processing gain. Optimized weights, however, continue to null second-order contributors, so performance improves, although slowly.

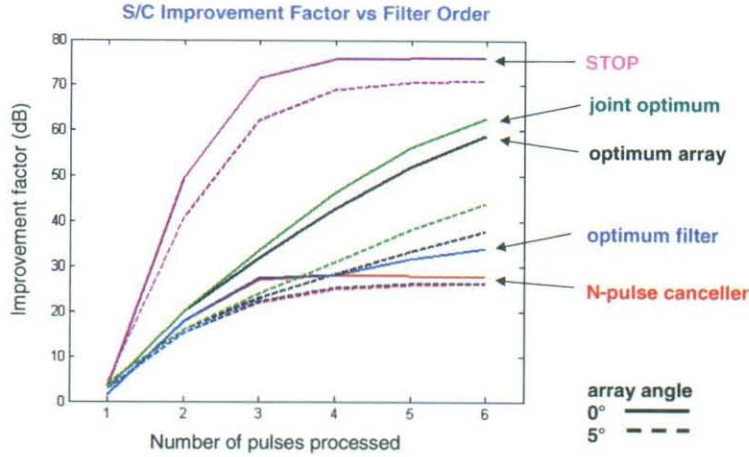


Figure 13. Signal/Clutter improvement factor vs. filter order for various alternatives of optimization.

A joint optimization of the array and filter weights can be achieved in an iterative fashion by alternating optimizing the a_m and w_n . Convergence is rapid and, although not guaranteeing a global maximum, leads to a maximum improvement factor attainable with separable space-time processing. The results shown in Fig. 13 represent only slight improvement over the optimized array with a simple N -pulse canceller.

7. Comparison with General Space-Time Processing

Finally, for reference, we compare separable processing with the ultimate case of space-time optimal processing (STOP), where each array element is followed by an individual Doppler filter. In contrast to separable processing which employs $M+N$ degrees of freedom, STOP employs $M \times N$ degrees of freedom. Performing an analysis as before, but now based on the full space-time clutter covariance matrix, leads to the results shown also in Fig. 13. The additional degrees of freedom clearly give superior improvement factors. When the number of pulses exceeds 3, the curves are noise-limited.

Our separable approach is critically based on a periodic array and a ‘tuned’ PRF. An interesting question therefore is whether the flexibility of general space-time processing can relieve this requirement for array periodicity.

To explore this question, we added random errors to the element location, such that they were distributed uniformly within a square 5 m box in the orbital plane and centered at the desired points. Assuming that the errors were known by independent measurements we then recomputed the S/C improvement factors for these arrays with perturbed periodicity. The results for two sample cases are shown in Fig. 14. Clearly even the general STOP solution benefits from a periodic array lattice.

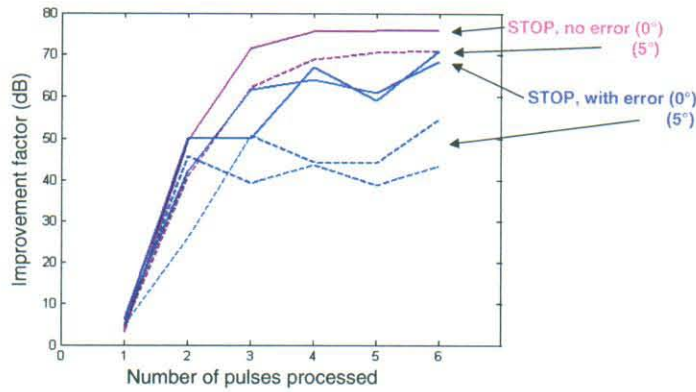


Figure 14. Comparison of Signal/Clutter improvement factors achievable with a periodic array and array with periodicity perturbed by random but known errors (two realizations).

8. Performance of the Planar Array under Non-Ideal Conditions

In the previous sections we have analyzed a vertical planar periodic array at one single, carefully chosen pulse repetition frequency, and have demonstrated this to be an ideal case with optimum clutter suppression. However, controlling the satellites to maintain the exact positions of a periodic grid may not be possible. Therefore we now analyze how performance degrades, first with array pitch and yaw and second, with random but known element position errors. We do this as a function of pulse repetition frequency, since this is our main free variable.

8.1. The Effects of Array Pitch and Yaw

We consider the same 19-satellite cluster as before, which forms a planar vertical array as shown in Fig. 6. For this array, ‘pitch’ implies that the velocity vector differs from the array axis direction but lies in the plane of the array. It is caused by the array rotating around its center during orbit. ‘Yaw’ implies a velocity component orthogonal to the plane of the array. It is caused by the Earth’s rotation.

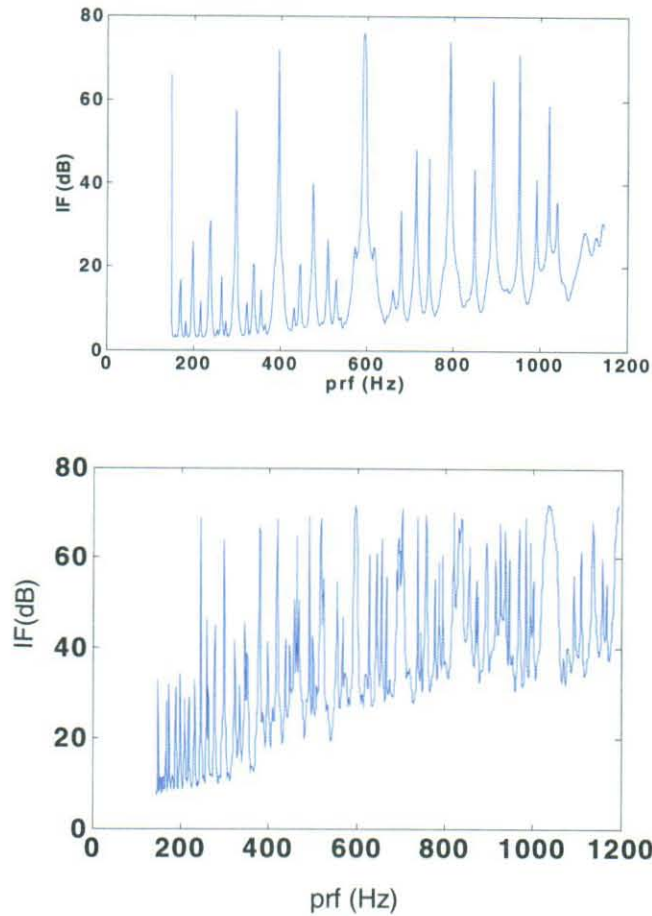


Figure 15.Improvement factor vs. pulse repetition frequency for the 19-element array with 0 deg. pitch, 0 deg yaw (top), and 5 deg. pitch, 0 deg. yaw (bottom).

For reference we show in Fig. 15 (top) the improvement factor (IF) vs. pulse repetition frequency for 0 deg. pitch and 0 deg. yaw. This is the optimal case. We note that there are many alternative prf values which give quite large IF values. However, these values sometimes have an extremely narrow bandwidth, e.g. for the peak at $\text{prf}=198$ Hz, a 0.005 Hz change makes a 10 dB difference. The reason is that the peaks essentially represent the difference between two large numbers, the clutter returns from two successive pulses. Since we cannot sample the curve densely enough these IF maxima are not always properly resolved, and in fact, the true IF maximum =73 dB at 198.027 Hz.

The lowest prf for which an IF maximum occurs corresponds to the situation when just the two edge elements of the array form a DPCA pair, i.e. at $\text{prf}=2 V_R/\Delta d = 148.5$ Hz, for a satellite velocity $V_R = 7425$ m/s and element distance $\Delta d = \text{aperture size} = 100$ m, which yields an IF =73 dB. At higher prf's some still larger IF values occur due to the simultaneous formation of several DPCA pairs.

Fig. 15(bottom) shows IF vs. prf when the array has a pitch angle of 5 deg., which represents one of the more difficult cases. We note that now there are many more IF maxima and also that the minima are less deep. This is due to the fact that the rotated array presents a larger set of interelement spacings and thus a larger set of DPCA pairs.

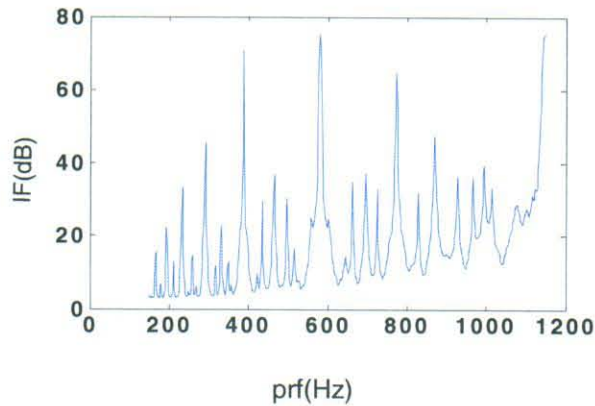


Figure 16. Improvement factor vs. pulse repetition frequency for the 19-element array with 0 deg. pitch, and yaw corresponding to Earth rotation.

Fig. 16 shows the effect of yaw due to Earth rotation. Apparently, this has very little effect on the IF curve. Presumably the reason is that the array elements are highly directive and thus the returns come essentially from the same direction, all with the same, relatively small, extra Doppler shift caused by the Earth rotation. The last observation that Earth rotation has only a minor effect holds also for a 5 deg. pitch angle.

8.2. Effects of Random Position Errors

In this section we investigate array performance degradation when the array (satellite cluster) can not be controlled to maintain a perfectly periodic grid. To model this situation we distribute the array elements randomly within square boxes, which are centered at the periodic grid points and contained in the single orbital plane of the array. Assuming the position errors are known, we again compute the improvement factor as a function of pulse repetition frequency for various error box sizes.

Fig. 17 shows the improvement factor vs. pulse repetition frequency for our 19-element array with 0 pitch and 0 yaw for error boxes 1, 3, and 5 m on the side, for one random but known realization. The case of 0 m box size, no position errors, shown in Fig.15 (top) above serves as a reference. With increasing position errors, the number of IF maxima increases while their peak values decrease. This is again because there is a richer set of element spacings, but, at any one frequency, only a small number of elements contribute to form DPCA pairs.

Finally, Fig. 18 shows IF results which include the effects of a 5 deg. pitch angle and yaw due to Earth rotation. Clearly the increased randomness, caused by the array rotation and the increasing error boxes, severely limits the attainable improvement factor. It is difficult to give an accurate estimate for this degradation due to the large dynamic range of the IF curves. However, it appears that random errors associated with the 5 m box cause an IF loss on the order of 10 dB compared with the ideal case with no position errors.

9. Conclusions

We have proposed a novel two-dimensional periodic array geometry for TechSat21 and an associated technique for pattern synthesis in angle-frequency space. It exploits the double periodicities of the grating lobes in the angular domain and of the radar pulses in the frequency domain, and allows substantial gains in clutter suppression.

We have considered a 'separable' system architecture for TechSat21, where a planar M -element array is followed by a single N -pulse Doppler filter, and have evaluated some processing alternatives for their effectiveness in clutter suppression. An attractive feature of this architecture is that it allows simple, multi-pulse MTI processing and adaptive antenna pattern control. The limited number of degrees of freedom, $M+N$, require a relatively low computational load.

General space-time processing offers substantially improved signal/clutter ratios. However, it employs a much larger number of degrees of freedom, $M \times N$, and may be associated with a computational load that is difficult to realize. Synthesis techniques for thinned apertures on transmit and receive, and the trade between performance and processing complexity merit further study.

Finally, taking the ideal periodic array as a reference case, we have analyzed the performance degradation with array pitch (satellite cluster rotation) and yaw (Earth rotation) and known random element position errors. We found that the signal/interference improvement factor is an extremely sensitive function of the pulse repetition frequency and that it varies over a large dynamic range. Achievable improvement factor maxima are moderately degraded by array pitch and strongly degraded with increasing position errors. Yaw effects appear to be negligible. In general, with increased randomness, fewer elements contribute to form DPCA pairs so that satellite usage efficiency (and SNR) is degraded.

Thus, a periodic array lattice allows for significantly better clutter suppression than a non-periodic lattice, independent of the particular space-time processing scheme.

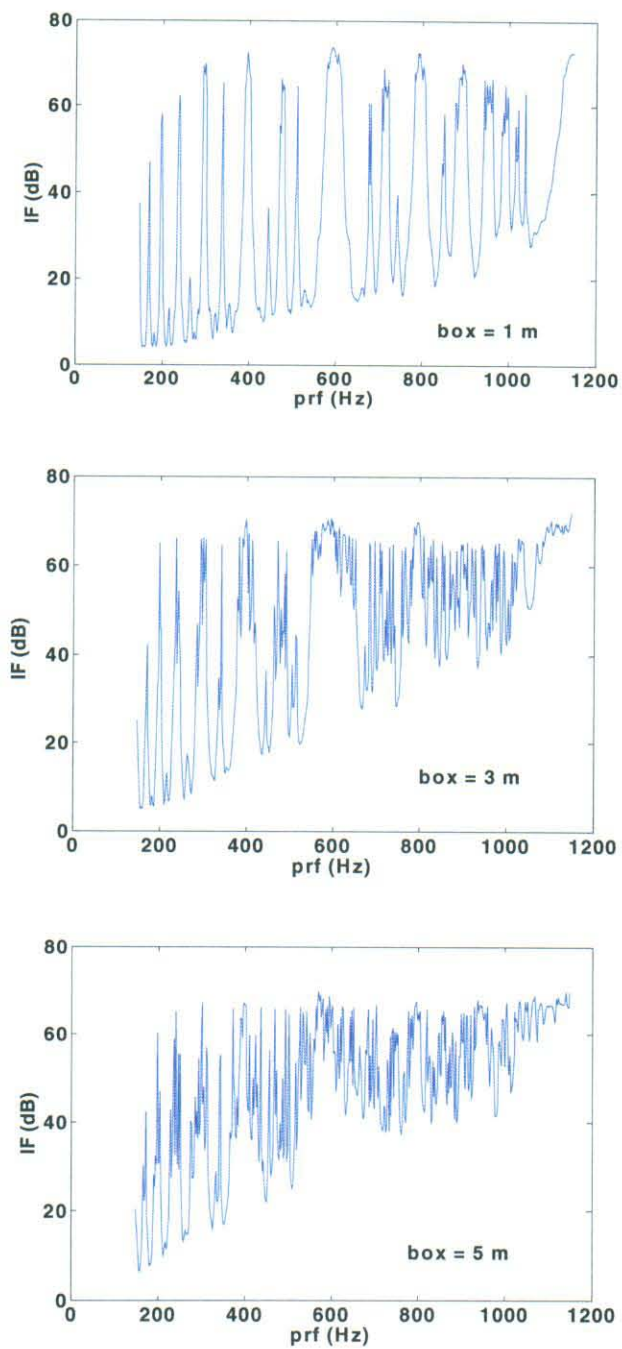


Figure 17. The improvement factor vs. pulse repetition frequency for random position errors within boxes 1, 3, and 5 m on the side (0 deg. pitch, 0 deg. yaw).

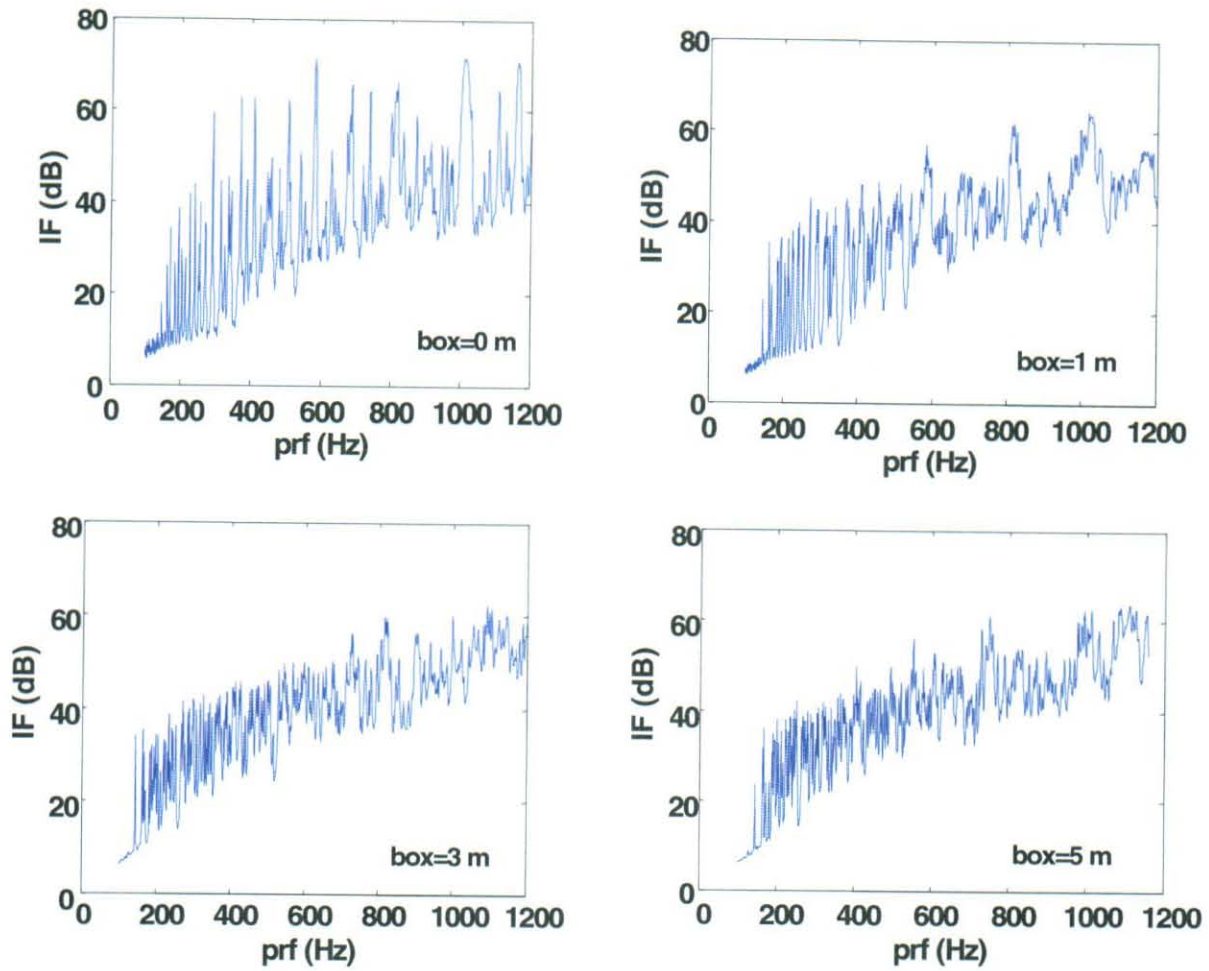


Figure 18. Improvement factor vs. pulse repetition frequency for the case of array pitch = 5° , yaw according to Earth rotation, and increasing element position errors.

10. References

- [1] Air Force Systems Command: *Executive Summary, Project Forecast*, 1986.
- [2] Air Force Research Laboratory: *TechSat21 - Next Generation Space Capabilities*. www.vs.afrl.af.mil/TechProgs/TechSat21, 1999.
- [3] R. J. Sedwick, T. L. Hacker, and K. Marais: *Performance Analysis for an Interferometric Space-Based GMTI Radar System*. IEEE International Radar Conference - RADAR 2000, May 2000.
- [4] J. H. G. Ender: *Spacebased SAR/MTI using Multistatic Satellite Configurations*. 4th European Conference on Synthetic Aperture Radar (EUSAR 2002), June 2002.
- [5] D. A. Leatherwood and W. L. Melvin: *Adaptive Processing in a Nonstationary Spaceborne Environment*. Proceedings of the IEEE Aerospace Conference, March 2003.
- [6] D. Massonnet: *Capabilities and Limitations of the Interferometric Cartwheel*. IEEE Transactions on Geoscience and Remote Sensing, vol. 39, no. 3, March 2001.
- [7] S. Ramongassie, et al.: *Preliminary Design of the Payload for the Interferometric Cartwheel*. 4th European Conference on Synthetic Aperture Radar (EUSAR 2002), June 2002.
- [8] H. Steyskal, J. K. Schindler, P. Franchi, R. J. Mailloux.: *Pattern Synthesis for TechSat 21 - A Distributed Space Based Radar System*. Proceedings of the IEEE Aerospace Conference, March 2001.
- [9] J. K. Schindler, H. Steyskal and P. Franchi: *Pattern Synthesis for Moving Target Detection with TechSat21 - A Distributed Space-Based Radar System*. Proceedings of IEE Radar 2002 Conference, Oct. 2002.
- [10] H. Steyskal, J. K. Schindler: *Separable Space-Time Pattern Synthesis for Moving Target Detection with TechSat 21 - A Distributed Space-Based Radar System*. Proceedings of the IEEE Aerospace Conference, March 2003.
- [11] H. Steyskal, J. K. Schindler, P. Franchi and R. J. Mailloux: *Pattern Synthesis for TechSat21 - A Distributed Space-Based Radar System*. IEEE Antennas and Propagation Magazine, Aug. 2003.
- [12] J. Dorey, Y. Blanchard, F. Christophe: *Le project RIAS, Une Approche Nouvelle du Radar de Surveillance Aerienne*. L'Onde Electrique, July-Aug. 1984.
- [13] J. Dorey et al: *RIAS, Radar a Impulsion et Antenne Synthetique*. Int'l Conf. on Radar, Paris, Apr. 1989.
- [14] J. Dorey, G. Garnier: *RIAS, Radar a Impulsion et Antenne Synthetic*. L'Onde Electrique, Nov.-Dec. 1989.

- [15] J. K. Schindler, H. Steyskal: *Sparse, Random Array Processing for Space-Based Radar*. Proceedings of the 36th IEEE Southeastern Symposium on System Theory, March 2004.
- [16] H. Steyskal, J. K. Schindler: *Beamforming and Signal Processing with Sparse, Random Arrays for Space Based Radar*. Proceedings of the IEEE Aerospace Conference, March 2004.
- [17] J. K. Schindler, H. Steyskal: *Transmit Beamforming and Waveforms for Random, Sparse Array Radar*. Proc. 2004 IEEE Waveform Diversity and Design Conf., Nov. 2004
- [18] J. K. Schindler: *Transmit Beamforming and Waveforms for Random, Sparse Array Radar*. AFRL Tech. Report to be published.
- [19] M. Martin, M. J. Stallard: *Distributed Satellite Missions and Technologies - The TechSat 21 Program*. AIAA Space Technology Conference and Exposition, Albuquerque, NM, Sept. 28-30, 1999
- [20] <http://www.interfacecontrol.com/papers/TechSat21MicroSats.pdf>
- [21] J. P. Prussing, B. A. Conway: *Orbital Mechanics*. Oxford University Press, 1993.
- [22] D. H. Johnson, D.E. Dudgeon: *Array Signal Processing*. Prentice-Hall, 1993.
- [23] R. J. Mailloux: *Phased Array Antenna Handbook*. Artech House, Inc., 2005

Appendix A

Comparison of Target Detection for Two Different Radar Modes

We show that the target detection performance against receiver noise of an array radar where each element transmits its own orthogonal signal can be equivalent to that of a conventional radar with a single coherent transmit signal. To this end we compare the total time required by the two systems to survey a given angular sector Ω_s , at a given signal-to-noise ratio.

Both systems are assumed to have an array of N elements with per element transmit power P_o , transmit gain G_t , receive gain G_r , and thermal receiver noise n_o . The element pattern beamwidth is Ω_o and the array beamwidth is Ω_a , with $\Omega_a \ll \Omega_o$ (see Fig. A1).

We consider a surveillance sector equal to the element beamwidth, $\Omega_s = \Omega_o$, which is motivated as follows. The satellite cluster constitutes a phased array where each element is one of the phased arrays on the individual satellites. Thus, in contrast to a conventional array whose element patterns are fixed in space, in the cluster array the element patterns can be redirected. However, once these directions have been set and the elements illuminate a fixed sector of width Ω_o then the cluster array is equivalent to a conventional array. Surveillance is then simply performed by scanning with the narrow cluster array beam of width Ω_a over the element pattern sector Ω_o . Surveillance over a sector larger than the element (satellite) pattern sector Ω_o is accomplished by step scanning the element pattern to contiguous sectors of width Ω_o .

1) *Conventional Radar Mode.* Here the array elements (satellites) transmit coherent pulsed signals all on the same carrier frequency. At the target, the illumination intensity is $\propto (NP_o)NG_t$, and for a fixed radar cross section, the power received is $\propto N^3 P_o G_t G_r$.

After coherent integration the receiver noise is n_o relative to the signal power received. Thus the signal-to-noise ratio $SNR \propto N^3 P_o G_t G_r / n_o$, and, assuming equal power and dwell time in each beam position, the total surveillance time is $\propto \Omega_o / \Omega_a$.

2) *Multi-Signal Mode.* In this case the elements (satellites) simultaneously transmit orthogonal signals, e.g. pulses on different carrier frequencies f_1 to f_N . It is assumed that the relative locations and pulse timings are so precisely known for each element that, after coherent demodulation, the complex video pulses corresponding to each orthogonal signal received at one element from one target direction can be combined coherently. Furthermore, it is assumed that the spread of carrier frequencies f_1 to f_N is not so large as to decorrelate the complex signal scattered by the target. In effect, this is coherent operation on transmit, and generates an effective illumination function equal to the array pattern. The following analysis assumes pulses transmitted on different carrier frequencies, f_1 to f_N , but applies as well for general orthogonal signals such as might be generated by orthogonal phase coding of the transmitted pulses.

Element 1 will illuminate the sector Ω_o with intensity $\propto P_o G_t$ at carrier frequency f_1 . The received signals at each of the N array elements from the element 1 transmission can be combined coherently to form a beam of width Ω_a with gain NG_r and a $SNR \propto NP_o G_t G_r / n_o$. However, since the entire sector Ω_o is illuminated, we can form a set of N contiguous receive beams within this

sector via digital beam forming. This process can be repeated at the frequencies f_1 to f_N , with one frequency transmitted from each of the N elements, thus allowing a total of N^2 independent receive beams. For the sparse array, the number of independent beam positions within the sector Ω_0 is not exactly N (~ 20) but rather on the order of 50, based on the size of the sparse array and the along-track aperture of the satellite array. This difference will be neglected here.

These beams can be employed in different ways:

- a) Form a cluster of N^2 contiguous beams. For the desired surveillance sector Ω_0 this leads to a surveillance time $\propto \Omega_0 / N^2 \Omega_a$ at a $\text{SNR} \propto NP_0 G_t G_r / n_0$. In comparison with the conventional radar mode, both the surveillance time and the signal to noise ratio are reduced by N^2 .
- b) Form, at each of the N frequencies, the same overlapping cluster of N contiguous receive beams, and add the N frequency signals at each beam output coherently. When compared to option (a), this leads to an increased surveillance time $\propto \Omega_0 / N \Omega_a$ at a proportionally increased $\text{SNR} \propto N^2 P_0 G_t G_r / n_0$. Thus, in comparison with the conventional radar mode, the surveillance time and the signal-to-noise ratio are reduced by N .
- c) Finally, integrating coherently N time samples from the above N beam clusters gives a surveillance time $\propto \Omega_0 / \Omega_a$ at a $\text{SNR} \propto N^3 P_0 G_t G_r / n_0$.

This last alternative shows that the conventional radar mode and the multi-signal mode give the same basic detection performance against receiver noise. However, the latter mode allows a trade of surveillance rate vs. SNR and longer integration times for Doppler processing to suppress clutter.

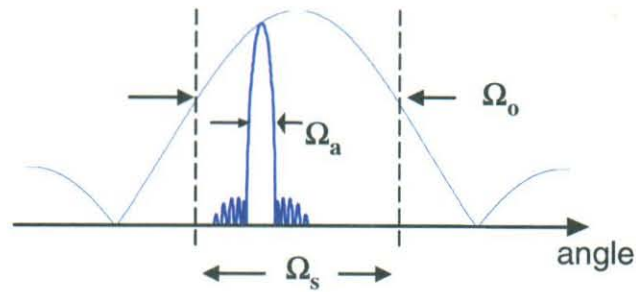


Figure A1. The element beamwidth Ω_0 is much wider than the array beamwidth Ω_a . Surveillance of a radar sector $\Omega_s = \Omega_0$ requires Ω_0 / Ω_a beams.

Appendix B

The Doppler Spectrum for Moving Targets and Clutter

B1. Aperture and Integration Time Requirements for Ground Moving Target Detection

Here we derive requirements on antenna aperture and coherent integration time to detect slowly moving ground targets.

We assume the radar has a horizontal velocity $\mathbf{v}_{\text{radar}}$ and illuminates one circular range cell at a depression angle δ , as shown in Fig. B1. The vector $\mathbf{v}_{\text{target}}$ denotes the target velocity relative to ground, and ψ is the angle between the target velocity and the direction $\hat{\mathbf{R}}$ to the radar. From the same azimuth angle φ we thus get two different Doppler returns due to the target motion, as illustrated in the Angle-Doppler diagram in Fig. B2.

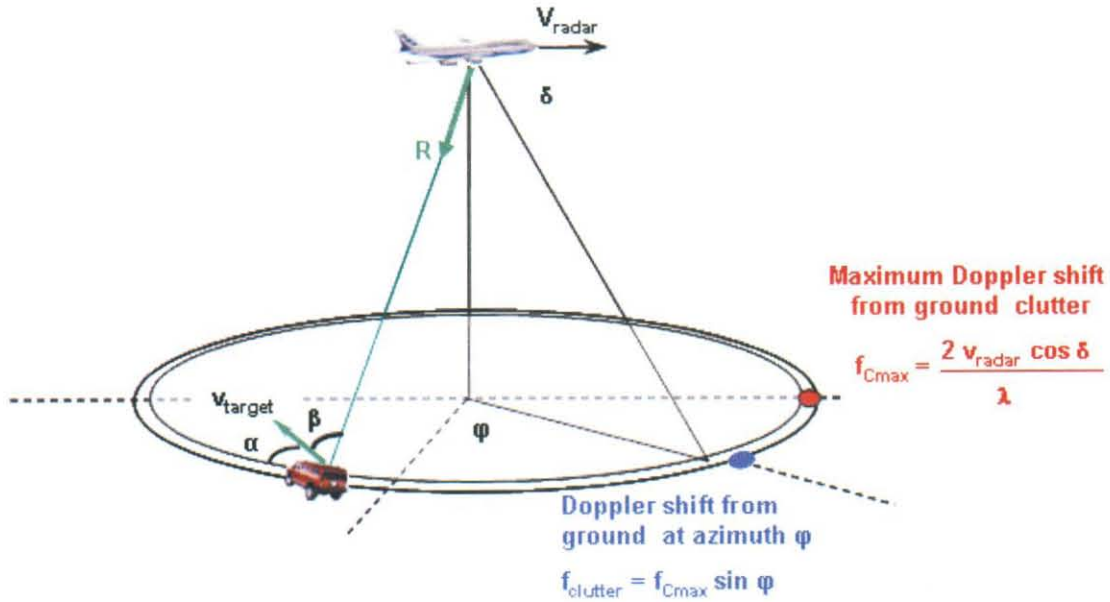


Figure B1. Illustration of radar and moving target geometry.

The Doppler frequency from ground clutter at azimuth angle φ is

$$f_{\text{clutter}} = \frac{2 \mathbf{v}_{\text{radar}} \cdot \hat{\mathbf{R}}}{\lambda} \quad (\text{B1})$$

leading to

$$f_{\text{clutter}} = f_{C\max} \sin \varphi \quad (\text{B2})$$

where

$$f_{C\max} = \frac{2 v_{\text{radar}}}{\lambda} \cos \delta. \quad (\text{B3})$$

The Doppler frequency for the target is similarly

$$f_{target} = \frac{2(\mathbf{v}_{radar} + \mathbf{v}_{target}) \cdot \hat{\mathbf{R}}}{\lambda} \quad (B4)$$

leading to

$$f_{target} = f_{clutter} + \frac{2v_{target}}{\lambda} \cos \beta. \quad (B5)$$

Defining the angle α between the vector \mathbf{v}_{target} and the tangent to the clutter cell we find that

$$\cos \beta = \cos \delta \sin \alpha \quad (B6)$$

and thus the Doppler differential Δf_{target} between the clutter and the target is

$$\Delta f_{target} = f_{target} - f_{clutter} = \frac{2v_{target}}{\lambda} \cos \delta \sin \alpha. \quad (B7)$$

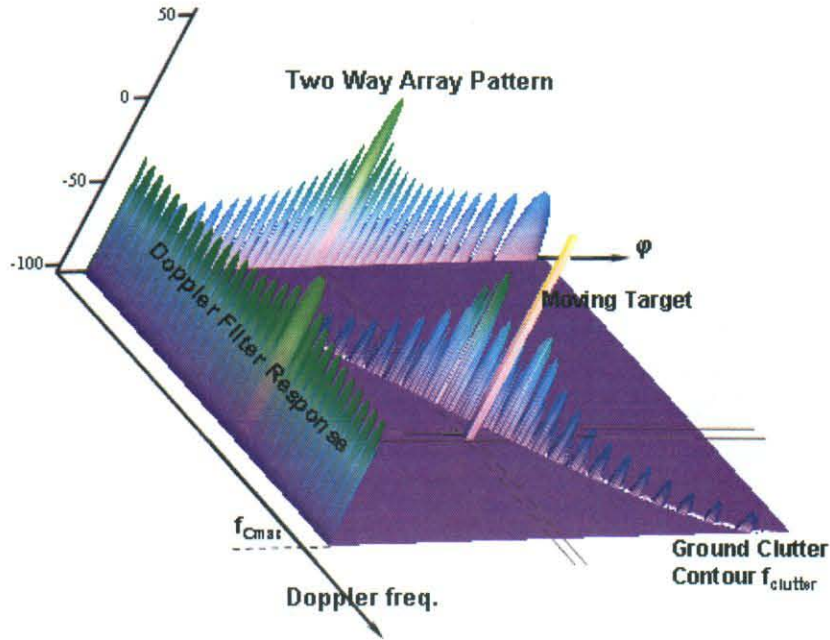


Figure B2. Target return and ground clutter return in Angle-Doppler space.

We can now estimate the minimum aperture size and integration time as illustrated in Fig. B3.

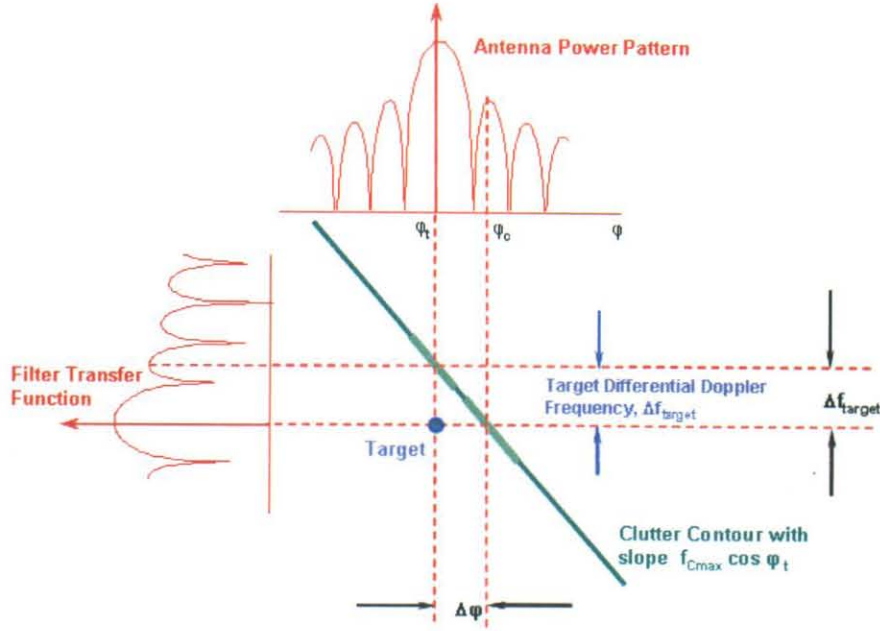


Figure B3. Illustrating the derivation of minimum aperture size and coherent integration time.

For a given Doppler differential Δf_{target} determined by the minimum detectable target speed we first require that the pass-band clutter be in the first sidelobe of the antenna pattern, i.e.

$$\Delta \varphi = \frac{3}{2} \frac{\lambda}{A_{\text{proj}}} \quad (\text{B8})$$

where $A_{\text{proj}} = A \cos \varphi$ is the projected antenna aperture and A is the aperture along the direction of $\mathbf{v}_{\text{radar}}$. From (B2) above we obtain

$$\frac{\Delta f_{\text{clutter}}}{\Delta \varphi} \approx f_{\text{Cmax}} \cos \varphi \quad (\text{B9})$$

and setting

$$\Delta f_{\text{clutter}} = \Delta f_{\text{target}} \quad (\text{B10})$$

we obtain from (B3) and (B7)

$$A = \frac{3}{2} \frac{v_{\text{radar}}}{v_{\text{target}} \sin \alpha} \lambda. \quad (\text{B11})$$

Similarly we require that the main-beam clutter be in the first sideband of the Doppler filter, i.e.

$$\Delta f_{target} = \frac{3}{2} \frac{1}{T} \quad (B12)$$

where T is the coherent integration time.

Using (B7) and (B8) leads to

$$T = \frac{3}{4} \frac{v_{radar}}{v_{target} \cos \delta \sin \alpha} \lambda . \quad (B13)$$

In (B11) and (B13) the dependence on the angles α and δ represent the unavoidable angular dependence of any Doppler detection scheme. Ignoring these factors we thus find for the minimum antenna aperture size

$$A \geq \frac{3}{2} \frac{v_{radar}}{v_{target}} \lambda \quad (B14)$$

and for the coherent integration time

$$D \geq \frac{3}{4} \frac{v_{radar}}{v_{target}} \lambda . \quad (B15)$$

B2. The Doppler Spectrum of Ground Clutter Seen from a Satellite in Earth Orbit

The Doppler frequency of the ground reflection as seen from a satellite in a circular Earth orbit is derived in [18] and repeated here for reference.

With the following notation

i = angle between orbital and equatorial planes, see Fig. B4

v = angular position of the satellite in the orbital plane, measured from the equator, see Fig. B4

R_e = radius of the Earth = 6378 km

h_s = height of the satellite above the surface of the Earth ≈ 850 km for our examples

μ_e = Earth gravitational constant = $3.986 \times 10^{14} \text{ m}^3 / \text{sec}^2$

ω_e = angular rate of Earth = $7.29 \times 10^{-5} \text{ rad/sec}$

φ = azimuth angle with respect to array broadside, see Fig. B4

δ = depression angle to the ground reflection point, see Fig. B4

dR/dt = line of sight distance change with time

λ = wavelength of radar signal

the Doppler frequency of the clutter is

$$f_D = -\frac{2}{\lambda} \frac{dR}{dt} = \frac{2}{\lambda} \left[\sqrt{\frac{\mu_e}{R_e + h_s}} \sin \varphi \cos \delta - \omega_e (R_e + h_s) (\sin \varphi \cos i - \cos \varphi \sin i \cos v) \cos \delta \right] \quad (\text{B16})$$

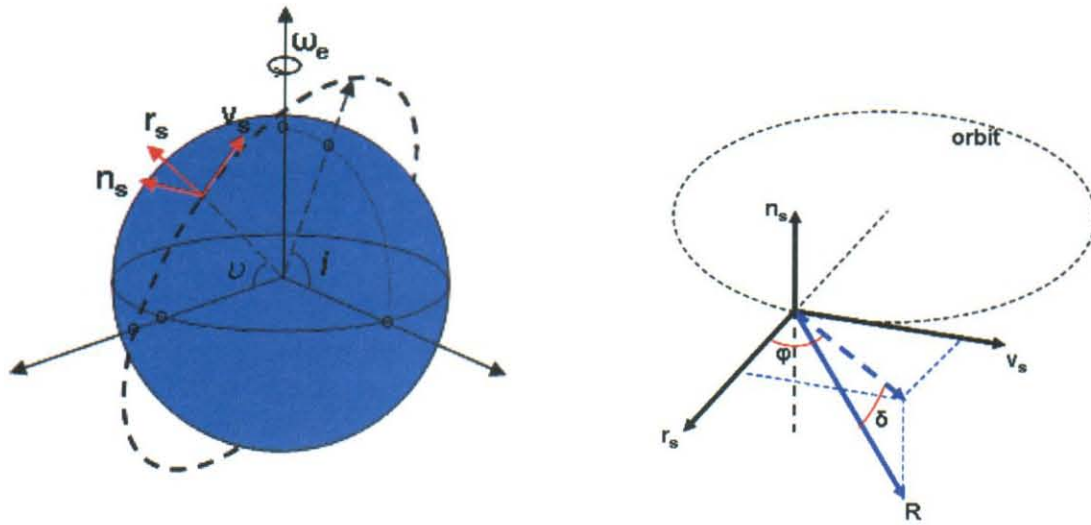


Figure B4. Global coordinate system and satellite-based coordinate system used in the computation of the clutter Doppler frequency (r_s and v_s are unit vectors along the radial direction to the satellite and along the satellite velocity, respectively, and $n_s = r_s \times v_s$).

Appendix C

Optimization of the Array Element Weights

In this appendix we derive the optimized array weights $\{a_m\}$, such that

$$\frac{P_{out}(\mathbf{a}, E^i = \text{signal})}{P_{out}(\mathbf{a}, E^i = \text{clutter}) + P_{out}(\text{noise})} = \max., \quad (\text{C1})$$

where P_{out} is the Doppler filter output power, E^i denotes the incident field on the array, and the Doppler filter weights $\{w_n\}$ are assumed given (see Fig. C1).

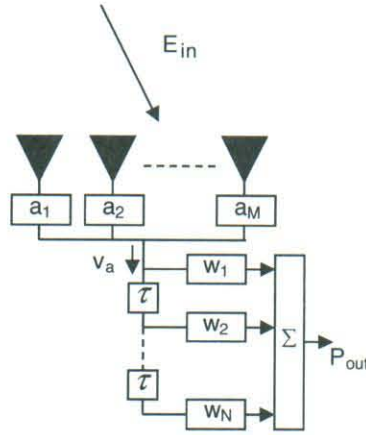


Figure C1. Array beam former with weights a_m followed by Doppler filter with weights w_n

We consider a plane wave $E^i(\varphi) e^{j(2\pi f t - \mathbf{k} \cdot \mathbf{r})}$ incident on an array with elements m located at \mathbf{r}_m . Here $f = f_0 + f_D$ denotes the sum of the basic carrier frequency f_0 and the Doppler frequency f_D . The direction of the wave vector \mathbf{k} denotes the direction φ of the wave*, and its magnitude $|\mathbf{k}| = 2\pi f / c$, where c is the speed of light. After demodulation (which essentially strips off the carrier frequency) the received signal at element m is $E^i(\varphi) e^{j(2\pi f_D t - \mathbf{k} \cdot \mathbf{r}_m)} e_0(\varphi)$, where $e_0(\varphi)$ denotes the element pattern with phase center at the origin (assumed equal for all elements). The array output voltage thus becomes

$$v_a(t, f_D) = E^i(\varphi) e^{j\omega_D t} e_0(\varphi) \sum_m a_m e^{-j\mathbf{k} \cdot \mathbf{r}_m}, \quad (\text{C2})$$

where a_m are the element weights.

*) The use of a single angular variable is justified since a range bin maps onto a very narrow sector in the array pattern, as discussed in the context of Fig. 8. Thus the total received clutter power can be obtained by integration over a single angular variable (the azimuth angle φ) along the sector, while assuming the power density being constant in the orthogonal direction.

In all following computations, we assume $\mathbf{k}(f) \cdot (\mathbf{r}_m - \mathbf{r}_n) \approx \mathbf{k}(f_0) \cdot (\mathbf{r}_m - \mathbf{r}_n)$, since the Doppler frequencies and range differences are sufficiently small.

Defining column vectors \mathbf{a} and Φ with components a_m and $e^{-j\mathbf{k} \cdot \mathbf{r}_m}$, respectively, we can write the amplitude

$$v_a(f_D) = E^i e_0(\varphi) \mathbf{a}^T \Phi(\mathbf{k}) . \quad (\text{C3})$$

The Doppler filter has the transfer function $w(f_D)$ so that the output voltage

$$v_{out} = w(f_D) v_a(\varphi, f_D) = E^i w(f_D) e_0(\varphi) \mathbf{a}^T \Phi(\mathbf{k}) . \quad (\text{C4})$$

For the target signal we assume the incident field $E^T e^{-j\mathbf{k}_T \cdot \mathbf{r}}$ to come from a single target direction φ_T with amplitude E^T uniformly distributed over the frequency interval $(0, f_{\text{rep}})$. This leads to a total output power

$$\begin{aligned} P_{out}^T &= \int_0^{f_{\text{rep}}} \left| w(f_D) e_0(\varphi_T) \mathbf{a}^T E^T \Phi(\mathbf{k}_T) \right|^2 df_D = \\ &= |E^T|^2 \mathbf{a}^T \left[|e_0(\varphi_T)|^2 \int_0^{f_{\text{rep}}} |w(f_D)|^2 \Phi \Phi^\dagger df_D \right] \mathbf{a}^* \end{aligned} \quad (\text{C5})$$

or

$$P_{out}^T = \mathbf{a}^T Q \mathbf{a}^* , \quad (\text{C6a})$$

where the elements q_{mn} of Q are

$$q_{mn} = |E^T|^2 |e_0(\varphi_T)|^2 \int_0^{f_{\text{rep}}} |w(f_D)|^2 e^{-j\mathbf{k}_T \cdot (\mathbf{r}_m - \mathbf{r}_n)} df_D . \quad (\text{C6b})$$

Recalling that $\mathbf{k}_T \cdot (\mathbf{r}_m - \mathbf{r}_n) \approx \mathbf{k}_T(f_0) \cdot (\mathbf{r}_m - \mathbf{r}_n)$ we obtain

$$q_{mn} \approx \text{constant} \times e^{-j\mathbf{k}_T(f_0) \cdot (\mathbf{r}_m - \mathbf{r}_n)} . \quad (\text{C7})$$

Thus the total target signal power

$$P^T = \mathbf{a}^T Q \mathbf{a}^* \propto \mathbf{a}^T \Phi(\mathbf{k}_T(f_0)) \Phi(\mathbf{k}_T(f_0))^\dagger \mathbf{a}^* . \quad (\text{C8})$$

The incident field due to clutter is spread over both angle φ and Doppler frequency f_D . However, we note that there is a one-to-one correspondence between φ and f_D , $\varphi = \varphi(f_D)$, and furthermore, the clutter signal is incoherent over φ .

The power contribution ΔP^C received from a sector $\Delta\varphi$ is proportional to the sector size, the clutter cross section per angle, σ_0 , (assumed constant), the relative illumination intensity given by the transmit power pattern $|F_t|^2$ and the receive power pattern $|F_r|^2$, i.e.

$$\Delta P^C \propto \sigma_0 |F_t(\varphi)|^2 \Delta\varphi |F_r(\varphi)|^2. \quad (C9)$$

Thus the received clutter power spectrum

$$S^C = \frac{\Delta P^C}{\Delta f_D} \propto \sigma_0 |F_t(f_D)|^2 |F_r(f_D)|^2 \frac{d\varphi}{df_D} \quad (C10)$$

or, with

$$\sigma_C(f_D) = \sigma_0 |F_t(f_D)|^2 \frac{d\varphi}{df_D}, \quad (C11)$$

$$S^C(f_D) \propto \sigma_C(f_D) |F_r(f_D)|^2 = \sigma_C(f_D) |e_0(f_D) \sum_m a_m e^{-j\mathbf{k} \cdot \mathbf{r}_m}|^2. \quad (C12)$$

Using similar vectors \mathbf{a} and Φ as before we obtain

$$S^C(f_D) \propto \sigma_C(f_D) |e_0(f_D)|^2 \mathbf{a}^t \Phi(f_D) \Phi(f_D)^\dagger \mathbf{a}^*. \quad (C13)$$

The matrix $M_\Phi(f_D) = \Phi(f_D) \Phi(f_D)^\dagger$ is computed numerically, as a function of frequency, by computing for each element location \mathbf{r}_m a set of values $e^{-j\mathbf{k}(f_{Dn}) \cdot \mathbf{r}_m}$, where the sample frequencies f_{Dn} extend over the entire Doppler spectrum. (The wave number $\mathbf{k}(f_{Dn})$ has magnitude $2\pi/\lambda_0$ and direction $\varphi = \varphi(f_{Dn})$).

The aliased Doppler spectrum S_{alias}^C is obtained as

$$\begin{aligned} S_{alias}^C &= \sum_{-\infty}^{\infty} S^C(f_D + \mu f_{rep}) = \\ &= \mathbf{a}^t \left[\sum_{-\infty}^{\infty} \sigma^C(f_D + \mu f_{rep}) |e_0(f_D + \mu f_{rep})|^2 M_\Phi(f_D + \mu f_{rep}) \right] \mathbf{a}^* \end{aligned} \quad (C14)$$

which leads to the total clutter output power

$$P_{out}^C = \int_0^{f_{rep}} |w(f_D)|^2 S_{alias}^C(f_D) df_D = \int_{-\infty}^{\infty} |w(f_D)|^2 S^C(f_D) df_D, \quad (C15)$$

since $w(f_D + \mu f_{rep}) = w(f_D)$ for all μ . Thus

$$P_{out}^C = \mathbf{a}' C \mathbf{a}^* \quad (C16a)$$

where the clutter matrix

$$C = \int_{-\infty}^{\infty} |w(f)|^2 \sigma_C(f_D) |e_0(f_D)|^2 M_{\Phi}(f_D) df_D. \quad (C16b)$$

Finally, adding thermal noise $P^N = \mathbf{a}' n_0 I \mathbf{a}^*$ to the clutter gives the signal-to-clutter+noise ratio

$$\frac{P_{out}^T}{P_{out}^C + P_{out}^N} = const. \times \frac{\mathbf{a}' \Phi(\mathbf{k}_T(f_0)) \Phi(\mathbf{k}_T(f_0))^{\dagger} \mathbf{a}^*}{\mathbf{a}' (C + n_0 I) \mathbf{a}^*} \quad (C17)$$

This ratio of quadratic forms is maximized by the weight vector

$$\mathbf{a} = \alpha [(C + n_0 I)^{-1} \Phi(f_0)]^*. \quad (C18)$$

Appendix D Doppler Filter Optimization

For an array followed by a Doppler filter, as shown in Fig. D1, we determine the filter weights w_n such that the signal-to-clutter ratio is maximized at the output of the Doppler filter. We use the following notation

- $v_{in}(f_D, t)$ = complex voltage at filter input
 $v_{out}(f_D, t)$ = voltage at filter output
 w_n = filter weights
 f_D = Doppler frequency
 τ = time between pulse samples, normally $\tau = 1/f_{rep}$, i.e. every consecutive pulse is used, however, setting $\tau = N_\tau / f_{rep}$ allows summation over every N_τ th pulse only.

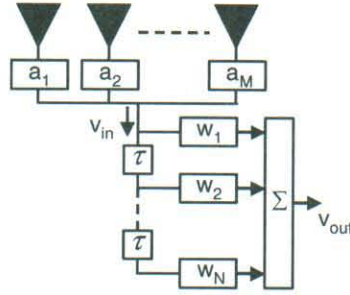


Figure D 1. Array with Doppler filter.

Sampling the demodulated input signal at times $t = (n-1)\tau$, $n=1,2,\dots, N$, and delaying and summing these pulses we obtain

$$v_{out}(f_D) = A(f_D) \sum_{n=1}^N w_n e^{j2\pi(n-1)f_D\tau} = \mathbf{w}^t \mathbf{v}_{in} \quad (D1a)$$

where

$$\begin{aligned} \mathbf{v}_{in}^t &= A(f_D)(1, e^{j2\pi f_D\tau}, \dots, e^{j2\pi(N-1)f_D\tau}) \\ \mathbf{w}^t &= (w_1, w_2, \dots, w_N). \end{aligned} \quad (D1b)$$

The output power spectrum S_{out} is proportional to the square of v_{out} , i.e.

$$S_{out} = |A(f_D)|^2 \mathbf{w}^t M \mathbf{w}^* \quad (D2a)$$

where the matrix

$$M(f_D) = \begin{pmatrix} 1 & e^{-j2\pi f_D \tau} & \dots & e^{-j2\pi(N-1)f_D \tau} \\ e^{j2\pi f_D \tau} & 1 & & \\ \dots & & & \\ e^{j2\pi(N-1)f_D \tau} & \dots & \dots & 1 \end{pmatrix}. \quad (D2b)$$

Now, assuming that the target Doppler frequency is uniformly distributed over the interval $(0, f_{\text{rep}})$, i.e. $A^T(f_D) = \text{constant}$, and, since $\tau = N_\tau / f_{\text{rep}}$, we obtain for the total target signal power

$$P^T = \int_0^{f_{\text{rep}}} S_{\text{out}}^T(f_D) df_D = |A^T|^2 \mathbf{w}^T \int_0^{f_{\text{rep}}} M(f_D) df_D \mathbf{w}^* = |A^T|^2 f_{\text{rep}} \mathbf{w}^T \mathbf{w}^*. \quad (D3)$$

Similarly, we obtain for the total clutter power

$$P_{\text{out}}^C = \int_0^{f_{\text{rep}}} S_{\text{out}}^C(f_D) df_D = \mathbf{w}^T \int_0^{f_{\text{rep}}} |A^C(f_D)|^2 M(f_D) df_D \mathbf{w}^* \quad (D4)$$

where $|A^C(f_D)|^2$ denotes the aliased clutter power spectrum at the filter input, as given by (C14).

The coefficients in the integral matrix $M_c = \int_0^{f_{\text{rep}}} |A^C(f_D)|^2 M(f_D) df_D$ are of the type

$$c_m = \int_0^{f_{\text{rep}}} |A^C(f_D)|^2 e^{jm2\pi f_D \tau} df_D \quad (D5)$$

and have to be evaluated numerically (they correspond to the Fourier-series coefficients of $|A^C(f_D)|^2$). With this notation we get

$$M_c = f_{\text{rep}} \begin{pmatrix} c_0 & c_{-1} & c_{-2} & \dots \\ c_1 & c_0 & c_{-1} & \dots \\ c_2 & c_1 & c_0 & \dots \\ \dots & \dots & \dots & \dots \end{pmatrix} \quad (D6)$$

which is Hermitian, since $c_{-m} = c_m^*$. The total output clutter power

$$P_{\text{out}}^C = \mathbf{w}^T M_c \mathbf{w}^*. \quad (D7)$$

We want to maximize the signal-to-clutter ratio, i.e. we seek a weight vector \mathbf{w} such that

$$\frac{P_{out}^T}{P_{out}^C} = \frac{|A_T|^2 f_{rep} \mathbf{w}^T \mathbf{w}^*}{\mathbf{w}^T f_{rep} M_c \mathbf{w}^*} = maximum \quad (D8a)$$

or, equivalently,

$$\frac{1}{\hat{\mathbf{w}}^T M_c \hat{\mathbf{w}}^*} = maximum \quad (D8b)$$

where $\hat{\mathbf{w}}$ denotes a weight vector of unit magnitude.

The solution to this maximization problem is given in terms of the eigenvectors \mathbf{e}_n and eigenvalues λ_n of M_c , [22], and is

$$\hat{\mathbf{w}} = \mathbf{e}_{\min}^* \quad (D9)$$

$$\left(\frac{P_{out}^T}{P_{out}^C} \right)_{\max} = \frac{|A_T|^2}{\lambda_{\min}}$$

where 'min' denotes the minimum eigenvalue and the corresponding eigenvector.

Appendix E Optimization of Space-Time Filter

In this appendix we derive the optimized weights $\{w_{mn}\}$ of a space-time filter, such that

$$\frac{P_{out}(\{w_{mn}\}, E^i = \text{target signal})}{P_{out}(\{w_{mn}\}, E^i = \text{clutter}) + P_{out}(\text{noise})} = \max., \quad (\text{E1})$$

where P_{out} is the filter output power and E^i denotes the incident field on the array (see Fig. E1).

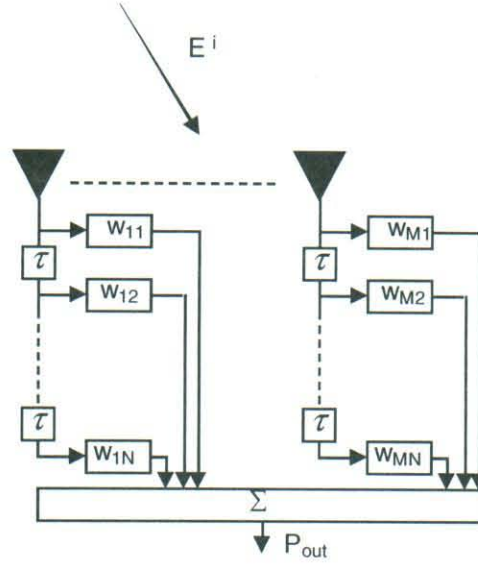


Figure E 1. Array with full space-time filter.

We consider a plane wave $E^i e^{-j\mathbf{k} \cdot \mathbf{r}}$ incident on an array with element m located at \mathbf{r}_m , as before. After demodulation the received voltage is at element m , time delay n

$$v_{mn} = v_m(t - (n-1)\tau) = E^i e_m(\varphi) e^{j2\pi f_D(t - (n-1)\tau)} \quad (\text{E2})$$

where the element pattern $e_m(\varphi) = e_0(\varphi) e^{-j\mathbf{k} \cdot \mathbf{r}_m}$ and $e_0(\varphi)$ denotes a common element factor.

The voltage output from the space-time filter

$$v_{out} = \sum_{m,n} w_{mn} v_{mn} = \mathbf{w}^T \mathbf{v} \quad (\text{E3})$$

where the $M \times N$ -dimensional vectors \mathbf{w} and \mathbf{v} have the components $w_\nu = w_{(m-1)N+n}$ and $v_\mu = v_{(m-1)N+n}$, respectively.

The total power received

$$P_{out} = \int_0^{f_{rep}} |v_{out}|^2 df_D = \mathbf{w}^T \int_0^{f_{rep}} \mathbf{v} \mathbf{v}^\dagger df_D \mathbf{w}^* \quad (\text{E4a})$$

or

$$P_{out} = \mathbf{w}^T \mathbf{M} \mathbf{w}^*, \quad (\text{E4b})$$

where the elements of the covariance matrix \mathbf{M} are

$$M_{\mu\nu} = \int_0^{f_{rep}} v_\mu v_\nu^* df_D. \quad (\text{E4c})$$

For the target we assume the signal to come from angle φ_T and be uniformly distributed over the Doppler range $(0, f_{rep})$, as before. This leads to a target covariance matrix \mathbf{M}^T with elements

$$\begin{aligned} M_{\mu\nu}^T &= \int_0^{f_{rep}} E^T e_{m(\mu)}(\varphi_T) e^{j2\pi f_D(t-(n(\mu)-1)\tau)} [E^T e_{m(\nu)}(\varphi_T) e^{j2\pi f_D(t-(n(\nu)-1)\tau)}]^* df_D = \\ &\approx |E^T e_0(\varphi_T)|^2 e^{-j\mathbf{k}_T(f_0) \cdot (\mathbf{r}_{m(\mu)} - \mathbf{r}_{m(\nu)})} \int_0^{f_{rep}} e^{-j2\pi(n(\mu)-n(\nu))f_D\tau} df_D = \\ &= |E^T e_0(\varphi_T)|^2 e^{-j\mathbf{k}_T(f_0) \cdot (\mathbf{r}_{m(\mu)} - \mathbf{r}_{m(\nu)})} \times \begin{cases} 1 & n(\mu) = n(\nu) \\ 0 & n(\mu) \neq n(\nu) \end{cases} \end{aligned} \quad (\text{E5})$$

For the clutter signal we note again the one-to-one correspondence between φ and f_D , $\varphi = \varphi(f_D)$, and that it is incoherent over φ .

Following an argument similar to that preceding (C12), where we showed that the received clutter power spectrum

$$S^C \propto \sigma_C(f_D) |F_r(f_D)|^2, \quad (\text{E6})$$

we obtain a corresponding received clutter voltage v_C at element m , time delay n

$$v_{C,mn}(f_D) \propto \sqrt{\sigma_C(f_D)} e^{j\Phi_C(f_D)} e_m(f_D) e^{j2\pi f_D(t-(n-1)\tau)}, \quad (\text{E7})$$

where Φ_C denotes clutter phase angle.

The elements of the clutter matrix \mathbf{M}^C are thus

$$\begin{aligned}
M_{\mu\nu}^C &= \int_{-\infty}^{\infty} \sigma_C(f_D) e_{\mu}(f_D) e_{\nu}(f_D)^* e^{-j2\pi f_D (n(\mu)-n(\nu))\tau} df_D = \\
&= \int_{-\infty}^{\infty} \sigma_C(f) |e_0(f_D)|^2 e^{-j\mathbf{k}(f_D) \cdot (\mathbf{r}_{m(\mu)} - \mathbf{r}_{m(\nu)})} e^{-j2\pi f_D (n(\mu)-n(\nu))\tau} df_D
\end{aligned} \tag{E8}$$

where $\mathbf{k}(f_D)$ denotes a wave vector with magnitude $2\pi / \lambda_0$ and direction corresponding to f_D .

Finally, adding thermal noise $P^N = \mathbf{w}' n_0 I \mathbf{w}^*$ to the clutter gives the signal-to-clutter + noise ratio

$$\frac{P_{out}^T}{P_{out}^C + P_{out}^N} = const. \times \frac{\mathbf{w}' A \mathbf{w}^*}{\mathbf{w}' B \mathbf{w}^*} \tag{E9}$$

where matrix $A = M^T$ and $B = M^C + n_0 I$.

The weight vector \mathbf{w}_{\max} that maximizes this ratio of quadratic forms is obtained by using a Singular Value Decomposition (SVD) to compute a matrix $B^{1/2}$ such that $B^{1/2} B^{1/2} = B$, $B^{-1/2} = (B^{1/2})^{-1}$. The desired weight vector is then given as

$$\mathbf{w}_{\max} \propto (B^{-1/2} \mathbf{e}_{\max})^* \tag{E10}$$

where \mathbf{e}_{\max} is the eigenvector corresponding to the largest eigenvalue of $(B^{-1/2})^+ A B^{-1/2}$.

Appendix F

Satellite Position Accuracy

The accuracy with which each satellite antenna phase center is known determines the quality of the grating lobe pattern formed by the TechSat21 sparse array. Uncompensated position errors remove power from the array grating lobes and distribute that power into inter-grating lobe angles or Doppler frequencies. Target detectability is degraded in these inter-grating lobe regions because of increased clutter power at Doppler frequencies competing with targets at these same frequencies. If the position errors become large enough, performance approaches that of the random sparse array discussed in the last section.

We assume that the satellites of the TechSat21 array are in a single orbital plane with an initial triangular grid described in Fig. 6b. The nominal motion of each satellite is governed by Kepler's equations for a spherical earth for satellites in a nearly circular orbit (eccentricities approximately 10^{-5}). Deviations from the nominal satellite positions will occur due to other forces such as residual atmospheric drag, and thruster and other gravitational forces. We assume that each satellite has onboard thrusters that maintain the satellite position within a control box which limits along-orbital-track position errors to be less than $\pm\epsilon$. Here ϵ is of the order of meters. Radial or cross-track control errors are less important since the sparse array electronic scan control can compensate for these errors at a constant radar range. The actual satellite position with respect to other satellites in the array is measured using laser ranging to provide relative positions with an error significantly less than a wavelength at the X band (10 GHz) carrier frequency of the radar. Thus, position errors of the satellites are modeled as deviations from the nominal positions having a random but known component on the order of meters and a random but unknown component on the order of 10^{-3} meters (≈ 0.1 wavelength).

The random but known position errors are used to electronically compensate the TechSat21 sparse array to form a beam in the pointing direction of the array. These known position errors cause grating lobes away from the pointing direction to degrade, as described above. This degradation becomes more severe for grating lobes farther away from the pointing direction of the array.

To assess bounds on the along-track position control error ($\pm\epsilon$), we require that there be no more than a 3 dB reduction in any sparse array average grating lobe within the main beam of the satellite pattern. Clutter power from increases in the inter-grating lobe pattern outside the satellite main beam will be reduced to a two-way sidelobe level of the satellite pattern. The random but known position error of each satellite is assumed to be uniformly distributed over the along track control box from $-\epsilon$ to $+\epsilon$ and independent of the position errors of the other satellites. Using this model, the reduction in average grating lobe gain of the one-way sparse array pattern due to position errors was computed. Allowing a gain reduction of 3 dB for a grating lobe at the first null of the satellite array pattern gives the following bound on the control error box:

$$\epsilon \leq 0.22L/B .$$

Here L is the along-track satellite aperture dimension and B is the azimuth beam-broadening factor [23] associated with the azimuth aperture distribution. Here $B=1$ corresponds to a

uniformly illuminated, maximum gain aperture and $B=1.2$, 1.36 , and 1.5 correspond to Chebyshev illuminations with -30 , -40 , and -50 dB one-way sidelobes, respectively. Fig. F1 shows this result. For a 2 m by 2 m satellite aperture, the control box varies from $\pm 0.3\text{ m}$ to $\pm 0.44\text{ m}$, depending on the beam-broadening factor. If the 4 m^2 satellite array aperture is conserved to provide adequate signal-to-noise but distributed as a $4\text{ m} \times 1\text{ m}$ aperture, the decreased azimuth beamwidth increases the control box to $\pm 0.6\text{ m}$ or $\pm 0.88\text{ m}$. This reduces the satellite thruster fuel consumption and increases mission lifetime.

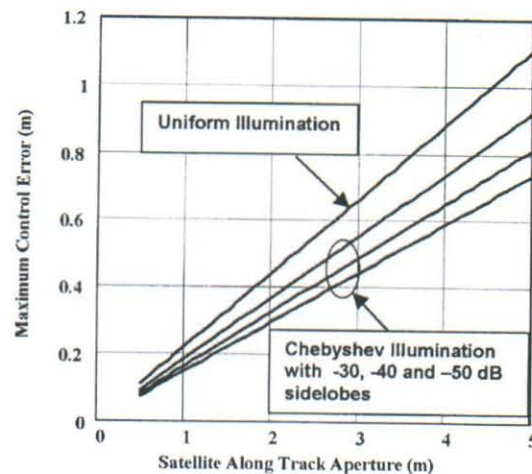


Figure F1. Maximum control error, ϵ , in meters vs. the satellite along track aperture, in meters, to insure that average sparse array grating lobes within the aperture main beam decrease less than 3 dB.